processes

MDPI

Article

Acid–Shale Interaction-Induced Pore–Fracture Reconstruction and Damage-Dependent Creep Evolution

Jiabao Yuan [1,2,3], Hai Huang [1,2,3,*], Zhengwei Liu [4], Zhuo Wang [4] and Hongxing Xu [5]

[1] College of Petroleum Engineering, Xi'an Petroleum University, Xi'an 710065, China
[2] Engineering Research Center of Development and Management for Low to Ultra-Low Permeability Oil & Gas Reservoirs in West China (Xi'an Petroleum University), Ministry of Education, Xi'an 710065, China
[3] Shaanxi Key Laboratory of Advanced Stimulation Technology for Oil & Gas Reservoirs, Xi'an Petroleum University, Xi'an 710065, China
[4] No.1 Oil Production Plant, PetroChina Changqing Oilfield Company, Yan'an 716009, China
[5] CCDC Changqing Down Hole Technology Company, Xi'an 710000, China
* Correspondence: huanghaixsyu@163.com

Abstract

Acid–shale interaction can substantially alter shale microstructure and time-dependent mechanical behavior, yet the link between mineral-scale reactions, pore–fracture reconstruction, and damage-dependent creep remains insufficiently quantified. Shale specimens were exposed to acidic solutions with initial pH values of 5, 3, and 1, followed by solution chemistry analysis, X-ray diffraction (XRD), nuclear magnetic resonance (NMR) T_2 relaxation analysis, scanning electron microscopy coupled with energy-dispersive X-ray spectroscopy (SEM–EDS), micro-computed tomography (micro-CT), and stepwise triaxial creep testing. A comprehensive damage variable D_c integrating mass loss, P-wave velocity degradation, and porosity increase was introduced to describe the post-reaction damage state independently of the mechanical parameters subsequently used in constitutive modeling. Preferential dissolution of calcite and dolomite weakened carbonate-bearing cement and promoted pore–fracture reconstruction. The total NMR porosity increased from 3.82% to 8.62%, while the long-T_2 (>100 ms) signal fraction increased from 5.5% to 18.0%. Correspondingly, the final cumulative axial strain increased from 0.687% to 2.480%, and the steady-state creep rate at 30 MPa increased from 1.55×10^{-4} to 10.40×10^{-4} h^{-1}. The estimated long-term strength threshold exceeded 30 MPa for the control shale but decreased to approximately 22 MPa after strong acid exposure. Incorporating D_c into a history-dependent viscoelastic–viscoplastic formulation enabled the progressive degradation of elastic stiffness, viscous resistance, and the nonlinear creep threshold to be described within a unified framework. Specimen-level cross-validation showed improved predictive performance relative to conventional Burgers and Nishihara models. The results therefore provide a quantitative state-to-response framework linking independently characterized acid-induced physicochemical damage to subsequent creep evolution.

Keywords: shale; acid–rock interaction; carbonate dissolution; pore–fracture reconstruction; creep deformation; long-term strength; damage-coupled constitutive model

Check for updates

Academic Editor: Liyun Yang

Received: 17 August 2026
Revised: 9 October 2026
Accepted: 23 October 2026
Published: 3 November 2026

Copyright: © 2026 by the authors. Licensee MDPI, Basel, Switzerland. This article is an open access article distributed under the terms and conditions of the Creative Commons Attribution (CC BY) license.

1. Introduction

Shale is a highly heterogeneous geomaterial whose mechanical behavior is governed by the coupled effects of mineral composition, bedding structure, pore–fracture architecture, and fluid–rock interaction. In unconventional hydrocarbon development, shale formations

are repeatedly exposed to drilling fluids, fracturing fluids, formation brines, acid-bearing fluids, and CO_2-rich fluids, making their mechanical properties dynamically dependent on the surrounding chemical environment [1]. Fluid invasion may alter the physicochemical state of the shale matrix through hydration, dissolution, ion exchange, and the redistribution of pore fluids, thereby affecting its stiffness, strength, permeability, and long-term structural integrity [2,3]. These effects are particularly important near wellbores and stimulated fractures, where chemically altered shale remains subjected to sustained in situ stress after drilling or hydraulic stimulation. Progressive weakening of bedding interfaces and pre-existing defects can consequently contribute to delayed borehole instability, fracture closure, and deterioration of fracture conductivity [4–6].

The interaction between reactive fluids and shale is fundamentally a multiscale process involving mineral reactions and subsequent reconstruction of the internal pore structure. Previous investigations of shale–fluid systems have demonstrated that fluid chemistry, salinity, redox conditions, and pH strongly influence mineral dissolution, secondary precipitation, fines migration, and the development of chemically altered zones [7–10]. Among these processes, carbonate-bearing shale is particularly sensitive to acidic fluids because calcite, dolomite, and carbonate-rich cement can dissolve rapidly when exposed to low-pH environments. Such reactions may enlarge existing flow pathways while simultaneously weakening intergranular cementation and local load-transfer structures [11]. Similar mineralogical and mechanical changes have been observed during CO_2–brine–rock interactions, where carbonic-acid-related reactions modify both the pore structure and mechanical properties of carbonate-rich shale [12]. Experiments on Longmaxi and other organic-rich shales further show that water-based, CO_2-based, and acid–CO_2 fluids can produce mineral dissolution, pore redistribution, microstructural degradation, and measurable deterioration of mechanical properties [13–16]. These observations indicate that the mechanical consequences of acid exposure cannot be represented solely by the initial acidity of the reacting fluid; rather, they depend on the post-reaction structural state produced by the coupled mineralogical and pore-scale changes.

This distinction becomes more important when time-dependent deformation is considered. Shale surrounding a wellbore or hydraulic fracture may remain under sustained differential or closure stress for periods far longer than those represented by conventional short-term strength tests. Under such conditions, progressive creep deformation can accumulate even when the applied stress remains below the short-term failure strength. Recent experiments have shown that acid corrosion can enhance creep and shear–creep deformation and reduce the long-term mechanical resistance of shale [17,18]. Chemo-mechanical simulations further suggest that dissolution and precipitation can modify internal stress-transfer pathways and generate time-dependent deformation through evolution of the solid skeleton [19]. Damage-controlled creep behavior has also been reported in organic-rich shale, where progressive microcrack interaction and internal deterioration strongly influence long-term deformation [20]. At smaller scales, nanoindentation and microindentation investigations have demonstrated that the creep response of shale is closely related to mineralogical heterogeneity, organic matter distribution, and the viscoelastic characteristics of individual mineral phases [21–25]. Together, these studies establish that shale creep is intrinsically multiscale and can be substantially modified by chemical alteration.

Despite this progress, the transition from acid–shale reaction to pore–fracture reconstruction and ultimately to macroscopic creep evolution remains incompletely quantified. A major limitation is that many experimental studies use initial pH, fluid type, or exposure duration as direct descriptors of chemical damage. These variables characterize the external reaction environment but do not uniquely represent the internal state reached after fluid–rock interaction. Shales subjected to the same exposure time may undergo different degrees

of mineral removal, wave-velocity degradation, porosity increase, and stiffness loss because of differences in mineral accessibility and reaction pathways. In addition, mineralogical and pore-structure observations are commonly interpreted separately from mechanical measurements, making it difficult to determine how dissolution-induced structural changes translate into increases in creep strain, steady-state creep rate, or reductions in long-term strength. Constitutive descriptions present a related challenge. Existing Burgers-type, Nishihara-type, thermodynamic, and nonlinear creep formulations provide useful representations of time-dependent rock deformation [26–30], but chemical damage is frequently introduced indirectly or model parameters are independently fitted for individual experimental conditions. Consequently, a unified state variable linking measurable physicochemical deterioration to pore–fracture reconstruction and damage-dependent creep parameters is still needed.

To address this issue, the present study investigates the evolution of shale from acid–rock reaction to structural degradation and time-dependent mechanical weakening. Shale specimens were exposed to acidic solutions with different initial pH values, and solution chemistry, X-ray diffraction (XRD), nuclear magnetic resonance (NMR) T_2 relaxation analysis, scanning electron microscopy coupled with energy-dispersive X-ray spectroscopy (SEM–EDS), and micro-computed tomography (micro-CT) were combined to identify the mineralogical and pore–fracture changes generated by acid exposure. Rather than treating preferential carbonate dissolution itself as a new mechanism, the present study focuses on quantifying how the post-reaction physicochemical damage state governs the subsequent time-dependent mechanical response. A composite damage variable D_c, constructed from mass loss, P-wave velocity degradation, and porosity increase independently of the mechanical parameters used in constitutive modeling, was introduced to describe the post-reaction state. Stepwise triaxial creep tests were then used to establish quantitative relationships between D_c, cumulative deformation, late-stage creep rate, and the estimated long-term strength threshold. Finally, a history-dependent viscoelastic–viscoplastic formulation was developed in which the damage state continuously controls stiffness, viscous resistance, and the stress threshold for nonlinear creep under stepwise loading. The principal contribution therefore lies in establishing and validating a quantitative state-to-response framework linking independently characterized physicochemical deterioration to history-dependent creep evolution, rather than in re-establishing the already recognized preferential dissolution of carbonate minerals.

2. Materials and Methods

2.1. Shale Sample Preparation and Grouping

The shale samples were obtained from the Chang 7_3 sub-member of the Upper Triassic Yanchang Formation in the Qingyang area of the southwestern Ordos Basin, China, at burial depths of approximately 2030–2060 m. The Chang 7 interval represents a typical continental lacustrine shale succession, with organic-rich laminated shale extensively developed in deep-lacustrine depositional settings [31]. The representative shale had a total organic carbon (TOC) content of 4.31 wt% and a vitrinite reflectance (R_o) of 1.02%, indicating a mature organic-matter evolution stage. Clay-mineral analysis showed that the clay fraction was dominated by illite/smectite mixed layers (I/S) and illite, with subordinate chlorite and kaolinite, consistent with the clay-mineral assemblage commonly reported for Chang 7 shale [32]. The principal geological, organic-geochemical, mineralogical, and sampling characteristics are summarized in Table 1. Cylindrical specimens with a diameter of 25 mm and a height of 50 mm were drilled from the same block, and the end faces were ground to ensure parallelism within 0.02 mm. The specimen axis was oriented normal to the bedding plane for all specimens ($\theta = 90°$, where θ denotes the angle between the specimen

axis and the bedding plane). This orientation was kept constant throughout the study so that bedding-related anisotropy was controlled rather than treated as an experimental variable. Samples with visible macroscopic fractures, edge damage or abnormal density were discarded. Before acid treatment, the dry mass, bulk density and P-wave velocity of each specimen were measured. Across the accepted cylindrical specimens, the mean initial bulk density was 2.51 ± 0.04 g/cm^3 and the mean initial P-wave velocity was 3020 ± 72 m/s (mean ± SD), confirming that the pre-test specimen variability remained within the screening criteria. Only specimens with a density variation less than 3% and initial P-wave velocity variation less than 5% were used for subsequent testing.

Table 1. Geological and compositional characteristics of the shale samples.

Parameter	Value or Description
Basin	Ordos Basin, China
Sampling locality	Qingyang area, southwestern Ordos Basin
Formation	Upper Triassic Yanchang Formation
Stratigraphic interval	Chang 7_3 sub-member
Burial depth/m	2030–2060
Lithology	Dark gray to black laminated shale
Depositional setting	Freshwater deep-lacustrine, predominantly subtoxic–reducing
TOC/wt%	4.31
Ro/%	1.02
XRD-normalized clay-mineral proportion/wt%	27.4
I/S/% of clay fraction	44.2
Illite/% of clay fraction	34.7
Chlorite/% of clay fraction	15.6
Kaolinite/% of clay fraction	5.5
Specimen orientation	Axis normal to bedding plane, θ = 90°

Specimen allocation was predefined before testing so that independent parallel specimens, rather than repeated measurements on the same specimen, constituted the experimental replicates. Separate specimen sets were used for physicochemical damage evaluation, creep testing, and microstructural characterization, and the specimen-identification scheme and corresponding measurements are summarized in Table 2.

The specimens were divided into one deionized-water control group (hereafter referred to as the control group) and three acid-treated groups. The control specimens were exposed to deionized water without added HCl, whereas the acidic solutions had initial pH values of 5, 3, and 1. Control and acid-treated specimens were subjected to the same exposure durations of 7, 14, and 21 days. Acidic solutions with initial pH values of 5, 3 and 1 were prepared using diluted HCl and deionized water. The exposure durations were set to 7, 14 and 21 days. For physicochemical damage evaluation and calculation of the comprehensive damage variable D_c, mass, P-wave velocity, and connected porosity were determined using corresponding parallel specimens at each exposure duration. Detailed mineralogical characterization, pore-structure analysis, microscopic observation and creep testing were performed on the 21-day treated samples because they provided clearly distinguishable damage states after prolonged acid–shale interaction. For all quantitative comparisons, three independent parallel specimens were included in each experimental condition ($n = 3$). Quantitative results derived from independent specimens were expressed as the mean ± standard deviation (SD) to characterize specimen-to-specimen variability. Repeated instrumental readings on the same specimen were averaged first and were not treated as independent replicates; statistical dispersion was calculated from the three independent specimens within each experimental condition. All three independent specimens were

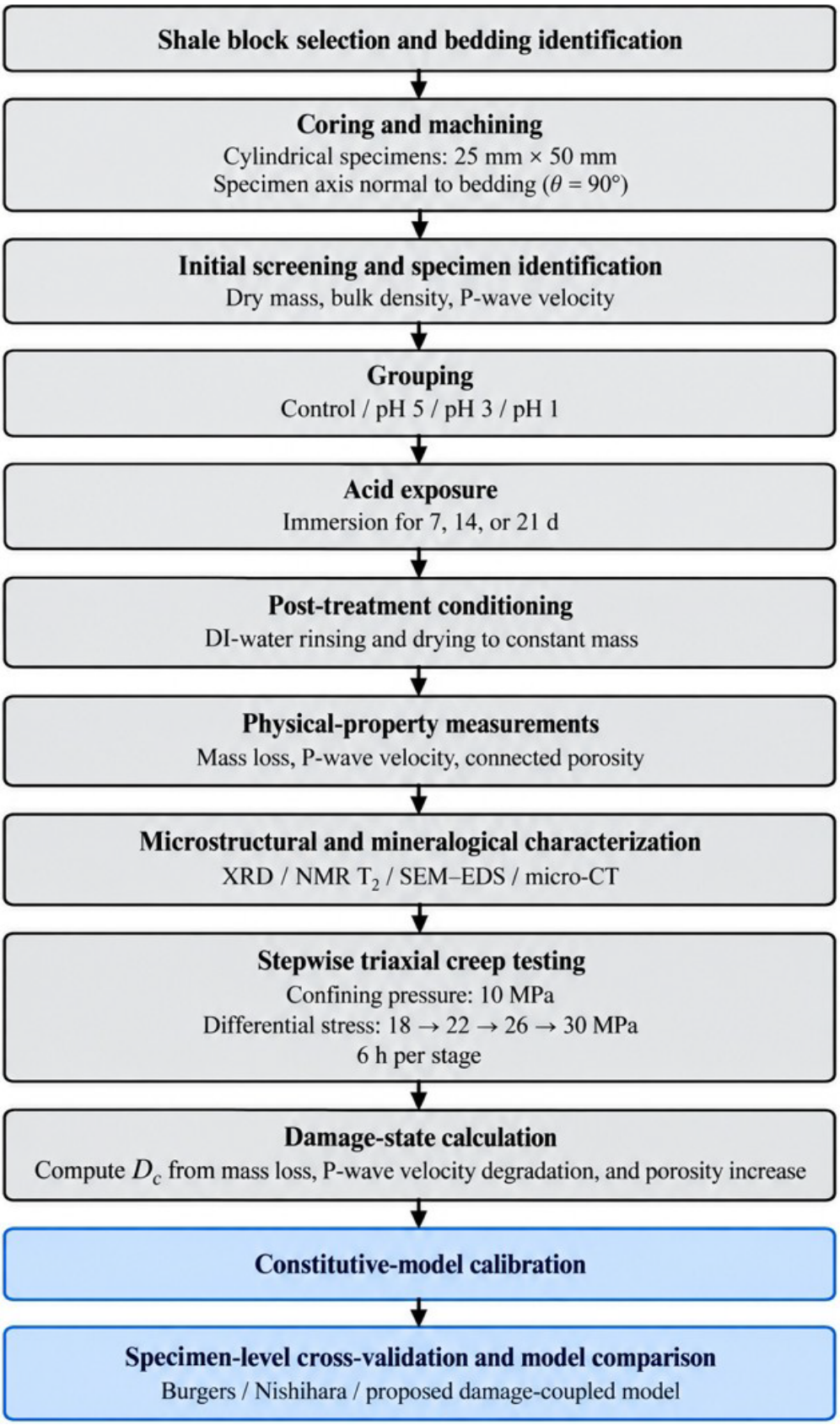
included in the creep analysis; no individual creep curve was selected as the representative quantitative response. The strain–time curves represent the pointwise mean of the three time-synchronized creep records, with the corresponding SD shown as an uncertainty band. Representative SEM–EDS and micro-CT images were selected from specimens whose bulk damage indicators were closest to the corresponding group mean; because these spatially resolved observations characterize local or representative structural features, they were used as complementary microstructural evidence rather than as independent observations for inferential statistical analysis.

Table 2. Specimen allocation and correspondence between specimen sets and experimental measurements.

Specimen Set	Specimen ID Format	Treatment Conditions	*n* per Condition	Main Measurements	Data Treatment
P-series	P-C/P5/P3/P1-7/14/21-R1–R3	Control, pH 5, pH 3, and pH 1; 7, 14, and 21 d	3	Mass change, P-wave velocity, connected porosity	Mean ± SD
M-series	M-C/P5/P3/P1-21-R1–R3	Control, pH 5 for 21 d, pH 3 for 21 d, and pH 1 for 21 d	3	NMR T_2 characterization; XRD and SEM–EDS on corresponding post-NMR fragments	Quantitative results from independent specimens; SEM–EDS used as local microstructural evidence
CT subset	M-C-21-R2; M-P1-21-R2	Control and pH 1 for 21 d end-member conditions	1 representative specimen per condition	Micro-CT	Descriptive end-member comparison; not used for inferential statistics
C-series	C-C/P5/P3/P1-21-R1–R3	Control, pH 5 for 21 d, pH 3 for 21 d, and pH 1 for 21 d	3	Stepwise triaxial creep, late-stage creep rate, estimated strength threshold, constitutive-model calibration/validation	Mean ± SD; specimen-level cross-validation

Note: C, P5, P3, and P1 denote the control, pH 5, pH 3, and pH 1 treatment groups, respectively; R1–R3 denote three independent replicate specimens.

After the prescribed exposure period, all specimens, including the control and acid-treated groups, were subjected to the same post-exposure procedure. The specimens were gently rinsed with deionized water to remove residual surface solution and then dried at 60 °C until the mass variation was less than 0.02% within 6 h. A drying temperature of 60 °C was used to avoid additional thermal alteration of the clay minerals. The creep tests were conducted on dried specimens to isolate the irreversible chemical damage from transient pore-pressure or capillary effects. The complete experimental workflow, including specimen screening and identification, group allocation, fluid exposure, post-treatment conditioning, physicochemical characterization, creep testing, and constitutive-model calibration and validation, is summarized in Scheme 1.



Scheme 1. Complete experimental workflow from specimen selection and preparation to physico-chemical characterization, stepwise triaxial creep testing, damage-state calculation, constitutive-model calibration, and specimen-level cross-validation/model comparison.

2.2. Acidic Exposure and Solution Chemistry

Each acid-treated specimen was immersed in the corresponding acidic solution in a sealed polyethylene container, whereas the time-matched control specimens were immersed in deionized water without added HCl under otherwise identical conditions. The liquid-to-solid ratio was maintained at 20 mL/g to ensure sufficient fluid contact during the reaction period. The liquid-to-solid ratio, container type, exposure temperature, exposure duration, and solution-handling procedure were identical for the control and acid-treated groups. The solutions were not renewed during exposure, so that the natural pH evolution could reflect acid consumption during shale–acid interaction. The containers were kept at 25 ± 1 °C. The solution pH was recorded at 0, 7, 14 and 21 days using PHS-3C laboratory pH meter (INESA Scientific Instrument Co., Ltd., Shanghai, China) with a resolution of 0.01 pH and an electronic-unit accuracy of ±0.01 pH.

After the designed exposure time, each specimen was removed, rinsed, dried and weighed. Dry mass was measured using an ME204E analytical balance (Mettler Toledo GmbH, Greifensee, Switzerland) with a readability of 0.1 mg. The mass loss ratio was calculated as:

$$D_m^{raw} = \frac{m_0 - m_t}{m_0} \times 100\% \quad (1)$$

where m_0 is the initial dry mass and m_t is the dry mass after acidic exposure.

The reacted solutions after 21 days were filtered through 0.22 μm membranes and acidified with trace HNO_3 before ion analysis. The concentrations of Ca^{2+}, Mg^{2+}, Al^{3+}, Fe^{3+}, Na^+, K^+ and dissolved Si were determined using an Agilent 5110 ICP-OES inductively coupled plasma optical emission spectrometry (ICP-OES) system (Agilent Technologies, Santa Clara, CA, USA). The instrument provides a typical long-term signal stability of <1% less than 1% relative standard deviation (RSD) under stable operating conditions. These ions were selected because they are directly related to carbonate dissolution, aluminosilicate alteration, and clay-mineral or feldspar-related reactions.

2.3. Ultrasonic Velocity, Porosity and Elastic Modulus Measurements

P-wave velocity was measured before and after acid exposure using an HS-YS301T rock ultrasonic parameter tester (Xiangtan Tianhong Electronic Research Institute, Xiangtan, China) equipped with 0.5 MHz longitudinal-wave transducers. The minimum acquisition interval was 0.05 μs. Coupling gel was applied at both ends of each specimen to improve acoustic contact. Each specimen was measured three times, and the mean value was used for subsequent analysis. Coupling gel was applied at both ends of the specimen to improve acoustic contact. Each sample was measured at least three times, and the average value was used. The P-wave velocity degradation ratio was calculated as:

$$D_v^{raw} = \frac{V_{p0} - V_{pt}}{V_{p0}} \times 100\% \quad (2)$$

where V_{p0} and V_{pt} are the P-wave velocities before and after acid exposure, respectively.

Porosity was determined by the vacuum-saturation method. Dried specimens were vacuumed for 6 h and then saturated with deionized water for 24 h. The saturated mass and dry mass were used to estimate connected porosity. For selected samples, NMR-derived porosity was used as an additional check. The elastic modulus was obtained from the initial linear portion of the stress–strain curve during mechanical loading. For consistency, the same stress interval was used for all specimens when calculating the elastic modulus. For the calculation of D_c, the corresponding P-wave velocity and connected porosity measurements were performed on parallel specimens from the 7-, 14-, and 21-day exposure groups together with the mass-loss measurements described above. Elastic modulus was retained as an independent mechanical response variable and was not included in D_c.

2.4. XRD Mineralogical Analysis

Representative fragments from the control and acid-treated shale samples were crushed, ground and passed through a 200-mesh sieve. X-ray diffraction analysis was conducted using a SmartLab X-ray diffractometer (Rigaku Corporation, Tokyo, Japan) with Cu Kα radiation. The scanning range was 5–70° in 2θ, with a step size of 0.02° and a scanning rate of 5°/min. The operating voltage and current were 40 kV and 40 mA, respectively.

The main mineral phases, including quartz, clay minerals, calcite, dolomite, feldspar and pyrite, were identified based on characteristic diffraction peaks. Semi-quantitative mineral contents were obtained using peak matching and whole-pattern fitting. The same phase-identification and whole-pattern fitting procedure was applied to all samples, and the fitted proportions of the identified crystalline phases were normalized to 100%. The resulting values therefore represent relative mineral abundances within each analyzed sample rather than absolute mineral mass losses. Because the XRD patterns of multiple samples were vertically offset for visual comparison, only relative peak changes within each pattern were used for qualitative interpretation. The normalized XRD phase proportions were interpreted together with gravimetric mass loss and solution chemistry to identify preferential mineral alteration. Because these proportions are normalized within each analyzed powder subsample, they were not used to calculate the absolute mineral mass loss or whole-specimen mineral mass balances.

2.5. NMR T_2 Relaxation Characterization

Low-field nuclear magnetic resonance measurements were performed using a MacroMR12-150H-I system (Niumag Analytical Instrument Co., Ltd., Suzhou, China), with a magnetic field strength of 0.30 ± 0.03 T, a nominal operating frequency of approximately 12 MHz, and a magnetic-field homogeneity of ≤50 ppm. Before testing, the specimens were dried, vacuumed for 6 h and saturated with deionized water for 24 h. The NMR tests were conducted using a Carr–Purcell–Meiboom–Gill sequence. The echo spacing was set to 0.2 ms, the waiting time to 3000 ms, and 32 scans were accumulated for each sample to improve the signal-to-noise ratio.

The T_2 relaxation spectra were used to compare the redistribution of water-associated relaxation components among different damage levels. For operational comparison, the spectra were divided into three relaxation-time domains: a short-T_2 domain ($T_2 < 1$ ms), an intermediate-T_2 domain ($1 \leq T_2 \leq 100$ ms), and a long-T_2 domain ($T_2 > 100$ ms). These fixed boundaries were only used to compare the relative redistribution of NMR signal among the tested samples. No direct conversion from T_2 to pore size was performed because T_2 depends on both pore geometry and surface relaxivity, and acid-induced changes in mineralogy and surface chemistry may alter the surface relaxivity. In addition, one-dimensional T_2 spectra were not used to infer pore connectivity. Total NMR porosity and the relative signal proportions of the three T_2 domains were calculated from the integrated NMR signal amplitude.

2.6. SEM–EDS Microscopic Characterization

SEM–EDS characterization was performed using a ZEISS Sigma 300 field-emission scanning electron microscope equipped with an EDS detector (Carl Zeiss Microscopy GmbH, Oberkochen, Germany). Small fragments were taken from the interior of each specimen to avoid cutting-surface contamination. The samples were dried at 60 °C and mounted on conductive adhesive tape. For morphology observation, the samples were sputter-coated with a thin gold layer. SEM images were acquired at an accelerating voltage of 5 kV under different magnifications to observe etched pores, mineral grain contacts, cementing regions and bedding-related microcracks.

For the SEM–EDS comparison, the control samples and those exposed to pH 1 for 21 d were selected as end-member states to highlight the contrast between the reference condition and the strongest acid-induced alteration. For EDS analysis, representative cementing regions and acid-etched areas were selected from the control and pH 1 for 21 d samples. To reduce interference from coating elements, the EDS specimens were carbon-coated when elemental spectra were collected. EDS spectra were acquired at an accelerating voltage of 15 kV. The relative changes in Ca, Mg, Si, Al and Fe were used to identify local carbonate dissolution and residual aluminosilicate enrichment. Since EDS analysis reflects selected local areas, the results were used as microscopic evidence rather than bulk mineral quantification.

2.7. Micro-CT Scanning and Fracture-Network Visualization

Micro-CT scanning was performed on the control and pH 1 for 21 d samples to visualize the three-dimensional contrast in fracture-network development between the two end-member damage states. Cylindrical specimens were scanned using a ZEISS Xradia 520 Versa three-dimensional X-ray microscope (Carl Zeiss X-ray Microscopy, Pleasanton, CA, USA). The system has a nominal spatial resolution of approximately 0.7 μm, whereas a voxel size of 5 μm/voxel was used in the present experiments to obtain a representative core-scale field of view. The tube voltage and current were set to 80 kV and 100 μA, respectively, and the voxel size was set to 5 μm/voxel. The sample was rotated through 360°, and projection images were collected at a rotation step of 0.3°. The reconstructed grayscale volume was obtained using filtered back-projection reconstruction.

A representative cylindrical region of interest was selected from the central part of each specimen to avoid edge artifacts. The grayscale slices were first inspected to identify internal discontinuities and fracture-like voids. The fracture phase was then extracted using grayscale threshold segmentation combined with manual correction. Small isolated noise components were removed before three-dimensional rendering. For descriptive quantification of the segmented volumes, the fracture volume fraction was calculated as the ratio of fracture voxels to total voxels within the region of interest, and the largest connected-cluster fraction was calculated as the volume of the largest connected fracture cluster divided by the total segmented fracture volume. The segmented fracture network was used to compare the control and strongly acid-treated samples. Because only the control and pH 1 for21 d specimens were scanned as end-member states, these metrics were used for descriptive comparison rather than inferential statistical analysis. Moreover, they represent only fracture-like features resolved at the 5 μm voxel scale and should not be interpreted as the total pore or microfracture volume of the shale.

2.8. Stepwise Triaxial Creep Testing

Stepwise triaxial creep tests were conducted using an MTS Model 815 servo-hydraulic rock-mechanics testing system (MTS Systems Corporation, Eden Prairie, MN, USA) equipped for triaxial loading. Each dried cylindrical specimen was enclosed in an impermeable jacket, centered between the upper and lower loading platens, and installed in the triaxial pressure vessel. Specimen alignment was checked before loading to minimize eccentric loading. After installation, the confining pressure was increased to 10 MPa and maintained until the pressure and axial-deformation signals stabilized. Differential stress was applied stepwise at 18, 22, 26 and 30 MPa. Each stress level was maintained for 6 h, giving a total creep duration of 24 h. The tests were conducted at 25 ± 1 °C.

The differential axial stress was increased between successive target levels at a constant loading rate of 0.05 MPa/s, while the confining pressure was maintained at 10 MPa throughout the test. Axial load, confining pressure, axial displacement, and axial strain were

acquired synchronously by the servo-control and data-acquisition system at a sampling interval of 1 s throughout the complete 24-h loading path. For group-level visualization, the three independent strain–time records obtained under the same loading program were temporally aligned, and the pointwise mean and SD were calculated throughout the test. For each loading stage, the instantaneous strain jump was separated from the subsequent time-dependent strain. The stage creep strain increment was defined as the strain increase during the constant-stress holding period after the instantaneous loading response. The final 2 h of each stress-holding stage were used to characterize the late-stage creep response. To determine whether this interval approached a quasi-steady condition, it was divided into four consecutive 0.5-h subintervals. A stage was regarded as quasi-steady only when the strain–time regression over the final 2 h yielded $R^2 \geq 0.98$ and the temporal trend of the four local creep rates was not statistically significant ($p \geq 0.05$). When these criteria were not satisfied, the calculated value was reported as an apparent late-stage creep rate rather than a steady-state creep rate.

2.9. Estimation of the Long-Term Strength Threshold

The long-term strength threshold was estimated by jointly considering the isochronous stress–strain response and the transition in late-stage creep rate. Isochronous stress–strain curves were constructed using strain values extracted at the same holding time from different stress stages. For each specimen, linear regressions were fitted to the quasi-linear response segments, and the change in slope was used together with the late-stage creep-rate response to constrain the transition stress. Because the differential stress was increased in 4 MPa increments, the resulting threshold was treated as an approximate transition estimate rather than as a precisely resolved material constant.

To identify the onset of accelerated-creep tendency objectively, the creep rate over the final 2 h of each loading stage was examined as a function of time. A stage was classified as exhibiting accelerated-creep tendency only when the slope of creep rate versus time was positive and statistically significant ($p < 0.05$). This criterion was used as an auxiliary check of the isochronous estimate rather than as evidence of fully developed tertiary creep. The experimentally constrained transition thresholds are reported to the nearest 1 MPa, consistent with the 4 MPa stress increment, while specimen-to-specimen uncertainty is represented by the corresponding SD ($n = 3$). For the control group, no transition was directly observed within the maximum applied differential stress of 30 MPa; therefore, its experimental threshold is reported as >30 MPa. The continuous fitted value of 31.8 MPa is retained only as an extrapolated parameter for constitutive-model calibration and is not interpreted as a directly measured long-term strength. For constitutive-model calibration and relative comparison, the degradation ratio based on the continuous fitted strength thresholds was calculated as:

$$D_\sigma = \frac{\sigma_{\infty,u} - \sigma_{\infty,t}}{\sigma_{\infty,u}} \times 100\% \quad (3)$$

where $\sigma_{\infty,u}$ and $\sigma_{\infty,t}$ are the continuous fitted strength thresholds of the unacidified control shale and acid-treated shale, respectively.

2.10. Comprehensive Acid-Induced Damage Variable

A comprehensive acid-induced damage variable D_c was defined to provide a unified descriptor of the post-reaction damage state and to link physicochemical alteration with the subsequent creep response. Three experimentally measurable non-mechanical indicators were used to construct D_c: mass loss, P-wave velocity degradation, and porosity increase. These indicators characterize material removal, loss of internal structural continuity, and pore–fracture development, respectively. Elastic-modulus reduction was excluded from the

revised definition of D_c to avoid mathematical dependence between the damage variable and the stiffness-related constitutive parameters subsequently analyzed. Because the three indicators have different units and characteristic ranges, each component was converted to a dimensionless form before integration:

$$D_c = \frac{1}{3}\left(D_m + D_v + D_\phi\right) \tag{4}$$

where D_m, D_v, and D_ϕ represent the normalized mass-loss damage, velocity damage, and porosity damage, respectively. The individual components were calculated as:

$$D_m = \frac{D_m^{raw}}{D_m^{ref}},\ D_v = \frac{D_v^{raw}}{D_v^{ref}},\ D_\phi = \frac{\phi_t - \phi_0}{D_\phi^{ref}} \tag{5}$$

where D_m^{raw} and D_v^{raw} are the unnormalized mass-loss ratio and P-wave velocity degradation ratio, respectively; ϕ_0 and ϕ_t are the porosities before and after acid exposure, respectively; and D_m^{ref}, D_v^{ref}, and D_ϕ^{ref} are the reference scaling values for mass loss, P-wave velocity degradation and porosity increase, respectively. In this study, these reference values were set to 10%, 50%, and 10 percentage points, respectively. These values were selected to cover the experimentally observed response ranges and to prevent differences in the numerical magnitudes of the three indicators from disproportionately affecting the integrated damage index. They are used solely as normalization scales and do not represent physical failure thresholds. Equal weighting was adopted after normalization as a neutral scheme because no independent experimental or theoretical basis was available for assigning preferential importance to mass loss, P-wave velocity degradation, or porosity increase. Equal weighting therefore minimizes additional subjective assumptions in the construction of D_c rather than implying that the three deterioration processes make physically identical contributions. Sensitivity calculations were performed by moderately perturbing the individual weighting coefficients and normalization factors. The resulting D_c values changed only within a limited range, while the relative damage ranking among the treatment groups remained unchanged, indicating that the classification of the post-reaction damage state is robust to reasonable variations in the weighting and normalization scheme. Accordingly, D_c is interpreted as an operational, dimensionless composite descriptor of the relative post-reaction physicochemical damage state rather than as an intrinsic material constant or a unique thermodynamic damage parameter. A higher D_c represents a greater combined degree of material loss, degradation of internal structural continuity, and pore-space development under the present experimental conditions. The framework is transferable in concept, whereas the normalization parameters should be recalibrated when applied to shale types with substantially different mineralogical, petrophysical, or structural characteristics. Absolute D_c values should therefore not be directly compared among different shale types unless a common normalization basis has been established. The resulting D_c was subsequently used to relate the post-reaction damage state to creep deformation, long-term strength and constitutive parameter evolution.

2.11. Damage-Coupled Creep Constitutive Model

A damage-coupled viscoelastic–viscoplastic creep model was used to describe the effect of acid-induced damage on shale creep behavior. Because the creep tests were performed under stepwise loading, the complete loading history was retained in the constitutive calculation rather than resetting the material state at each stress stage. The Burgers-type viscoelastic response was calculated by superposition of the successive stress increments. For the four loading stages, $\sigma_0 = 0$, $\sigma_1 = 18$ MPa, $\sigma_2 = 22$ MPa, $\sigma_3 = 26$ MPa, and $\sigma_4 = 30$ MPa, with $\Delta\sigma_j = \sigma_j - \sigma_{j-1}$ and stage-start times $t_1 = 0$ h, $t_2 = 6$ h, $t_3 = 12$ h, and $t_4 = 18$ h. At any global test time t within loading stage k, the cumulative axial strain was expressed as:

$$\varepsilon(t, D_c) = \sum_{j=1}^{k} H(t - t_j)\left[\frac{\Delta\sigma_j}{E_1(D_c)} + \frac{\Delta\sigma_j}{E_2(D_c)}\left\{1 - \exp\left[-\frac{E_2(D_c)}{\eta_2(D_c)}(t - t_j)\right]\right\} + \frac{\Delta\sigma_j}{\eta_1(D_c)}(t - t_j)\right] + \varepsilon_{\mathrm{vp}}(t, D_c) \quad (6)$$

where ε is the cumulative axial strain, t is the global test time, $\Delta\sigma_{\mathrm{j}}$ is the stress increment applied at the beginning of stage j, t_{j} is the corresponding stage-start time, and $H(t - t_{\mathrm{j}})$ is the Heaviside function. $E_1(D_{\mathrm{c}})$ is the instantaneous elastic modulus, whereas $E_2(D_{\mathrm{c}})$, $\eta_2(D_{\mathrm{c}})$, and $\eta_1(D_{\mathrm{c}})$ describe the delayed elastic and viscous responses. Stress-increment superposition ensures that the delayed viscoelastic response generated during each preceding loading stage is retained after subsequent stress increments are applied. Therefore, strain accumulated during an earlier stage is neither discarded nor reintroduced as a new response to the total stress.

The nonlinear viscoplastic strain was updated continuously across stage boundaries rather than recalculated from zero. For the current stage k ($t_{\mathrm{k}} \le t < t_{\mathrm{k+1}}$), it was evaluated as:

$$\varepsilon_{vp}(t, D_c) = \varepsilon_{vp}(t_k^-, D_c) + H[\sigma_k - \sigma_\infty(D_c)]A(D_c)[\sigma_k - \sigma_\infty(D_c)]^n(t - t_k)^m \quad (7)$$

where $\varepsilon_{vp}(t_k^-, D_c)$ is the irreversible viscoplastic strain accumulated up to the end of the preceding loading stage. Thus, only the local elapsed time of the newly activated viscoplastic contribution is reset at a stage boundary, whereas the accumulated internal strain state is carried forward. The viscoplastic contribution is activated only when $\sigma\square$ exceeds the damage-dependent threshold $\sigma_\infty(D_{\mathrm{c}})$. This formulation was used to describe the early accelerated-creep tendency observed at high damage and stress levels rather than to represent fully developed tertiary creep failure.

Because the control shale still had a small calculated damage variable, it was not treated as a theoretical zero-damage material. The damage-dependent degradation of each parameter was normalized by the corresponding value of the control sample:

$$\frac{P(D_c)}{P_u} = \exp[-\lambda_P(D_c - D_{c,u})] \quad (8)$$

where $P(D_{\mathrm{c}})$ denotes E_1, E_2, η_1, η_2 or σ_∞, P_{u} is the corresponding parameter of the unacidified control shale, $D_{\mathrm{c,u}}$ is the damage variable of the control shale, and λ_{P} is the damage-sensitivity coefficient. For the viscoplastic coefficient, a monotonic damage-enhancement form was adopted:

$$A(D_c) = A_u\exp[\lambda_A(D_c - D_{c,u})] \quad (9)$$

where A_{u} is the coefficient for the unacidified control shale and λ_{A} represents the sensitivity of viscoplastic deformation to acid-induced damage. The exponents n and m were treated as global fitting parameters to avoid over-parameterization. This formulation keeps the model compact while allowing stiffness degradation, viscous weakening and long-term strength reduction to be governed by the same damage variable.

2.12. Parameter Fitting and Model Evaluation

The model parameters were determined using nonlinear least-squares regression. Following completion of physicochemical characterization and creep testing, the measured mass-loss, P-wave-velocity, and porosity responses were used to calculate D_{c}, and the complete 24-h creep records were subsequently used for constitutive-parameter calibration and specimen-level cross-validation, as summarized in Scheme 1. For each specimen, the entire 24-h stepwise loading history was simulated in a single forward calculation using the stress-increment superposition and internal-variable update described in Section 2.11; individual stress stages were not fitted independently. Parameter bounds were imposed to ensure positive elastic moduli, viscosity coefficients, long-term strength, and viscoplastic coefficients. To limit parameter redundancy and reduce overfitting, n and m were treated

as global parameters shared across all damage levels, whereas E_1, E_2, η_1, η_2, and σ_∞ were linked to D_c through the damage-dependent degradation functions.

Model performance was quantitatively assessed using the coefficient of determination (R^2), root mean square error (RMSE), and mean absolute error (MAE):

$$\begin{aligned} R^2 &= 1 - \frac{\sum_{i=1}^{N} (y_i - \hat{y}_i)^2}{\sum_{i=1}^{N} (y_i - \overline{y})^2} \\ RMSE &= \sqrt{\frac{1}{N} \sum_{i=1}^{N} (y_i - \hat{y}_i)^2} \\ MAE &= \frac{1}{N} \sum_{i=1}^{N} \left| y_i - \hat{y}_i \right| \end{aligned} \tag{10}$$

where y_i is the measured cumulative axial strain, $\hat{y}_i$ is the predicted value, $\overline{y}$ is the average measured value and N is the number of validation points. Model calibration and validation were separated at the specimen level using threefold leave-one-specimen-out cross-validation. In each fold, one independent specimen from each damage group was withheld for validation, while the remaining two specimens were used for parameter calibration; the held-out specimens were not involved in parameter estimation. Parameter uncertainty was assessed by bootstrap resampling of the calibration specimens, and practical parameter sensitivity and identifiability were examined by ±10% one-at-a-time parameter perturbation together with bootstrap parameter correlations. For benchmark comparison, conventional Burgers and Nishihara models were calibrated and evaluated using exactly the same specimen-level cross-validation partitions and the same 24-h stepwise loading histories as the proposed model. The classical Nishihara model consisted of elastic, delayed-elastic, and yield-dependent viscoplastic components, whereas neither benchmark model incorporated the experimentally determined D_c-dependent parameter evolution used in the proposed formulation. For the experimental datasets, statistical analysis was performed using independent specimens rather than repeated instrumental readings. Quantitative data are reported as mean ± SD ($n = 3$). For variables evaluated as functions of both initial acidity and exposure duration, including mass loss and the comprehensive damage variable Dc, two-way analysis of variance (ANOVA) was used to assess the effects of initial pH, exposure time, and their interaction. For comparisons among the control, pH 5 for 21 d, pH 3 for 21 d, and pH 1 for 21 d groups, one-way ANOVA followed by Tukey's honestly significant difference (HSD) post hoc test was applied to quantitative endpoints including P-wave velocity degradation, creep strain increment, late-stage creep rate. Statistical significance was defined at $p < 0.05$. Inferential statistical testing was restricted to quantitative measurements obtained from independent specimens, whereas SEM–EDS and micro-CT observations were interpreted descriptively because of their spatially localized and representative nature.

3. Results and Discussion

3.1. Physicochemical Damage Evolution of Shale Under Acidic Exposure

Acidic exposure produced a progressive deterioration in the shale samples, as reflected by mass loss, pH neutralization, ion release and ultrasonic velocity degradation. The response was strongly dependent on the initial acidity, but it did not increase in a strictly linear manner with exposure time. Across the three acid-treated groups, most physicochemical changes developed rapidly during the first 7 days and then continued at a slower rate from 7 to 21 days. Such a pattern suggests that the early stage was mainly associated with the reaction between the acid solution and readily accessible mineral surfaces, while the later stage

was more likely affected by fluid penetration into less connected pores, bedding-related defects and newly opened microcracks.

As shown in Figure 1a, the time-matched control group showed only a small mass variation of 0.16% after 21 days, indicating that deionized-water exposure together with the subsequent rinsing and drying procedure produced substantially less material loss than the acid-treated conditions. In contrast, clear mass reduction occurred in all acid-treated groups. Under the weakly acidic condition of pH 5, the mass loss increased from 0.42% after 7 days to 0.91% after 21 days. When the initial pH decreased to 3, the corresponding values increased to 1.18%, 1.74% and 2.21% after 7, 14 and 21 days, respectively. The strongest alteration appeared in the pH 1 group, where the mass loss reached 2.36% after 7 days and further increased to 4.68% after 21 days. The difference between the pH 3 and pH 1 groups became more pronounced with longer exposure, pointing to the cumulative effect of strong acidity on the dissolution of acid-sensitive components. Nevertheless, mass loss alone cannot fully describe the internal damage state, because acid reaction along bedding planes and pre-existing defects may weaken the rock framework without producing proportional material removal.

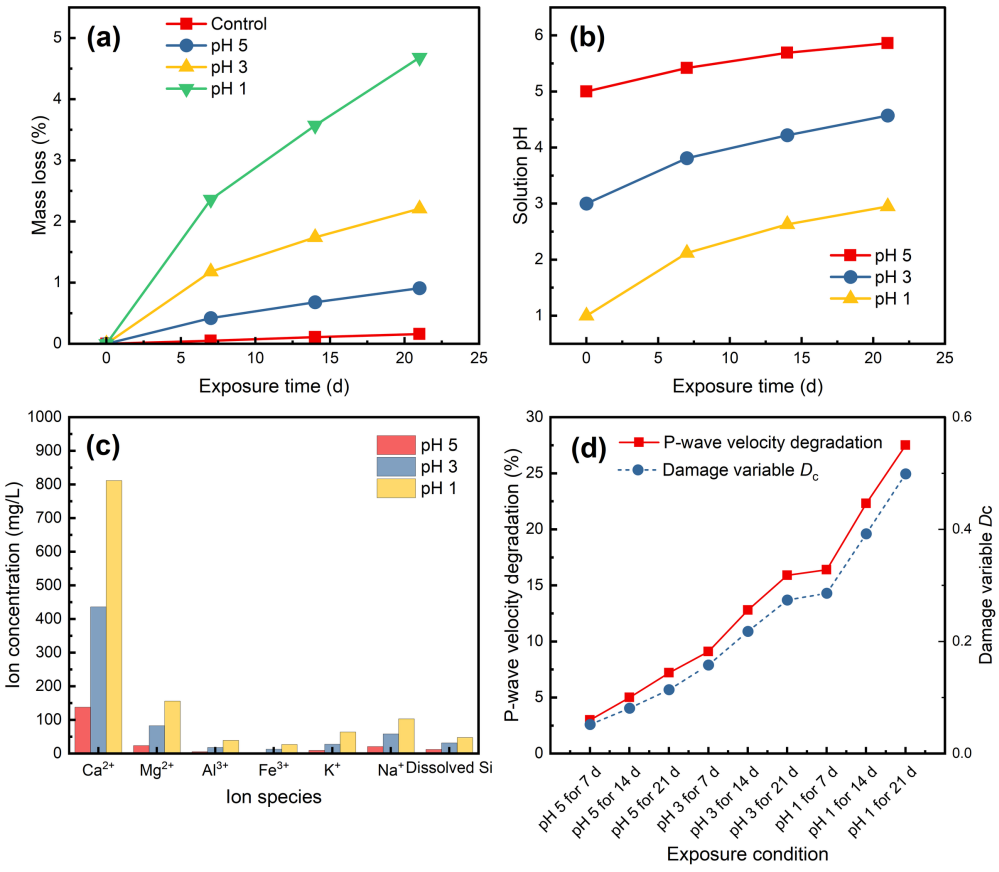


Figure 1. Physicochemical damage evolution of shale under acidic exposure: (**a**) mass loss during acid exposure; (**b**) pH evolution of acidic solutions; (**c**) ion concentration after 21 days of exposure; and (**d**) P-wave velocity degradation and comprehensive damage variable D_c under different acid-induced damage levels. Data are presented as mean ± SD ($n = 3$). For variables evaluated as functions of treatment condition and exposure duration, statistical significance was assessed by two-way ANOVA followed by Tukey's HSD post hoc test.

The pH evolution of the reacted solutions provides a complementary record of acid consumption during shale–acid interaction. As presented in Figure 1b, the pH of the initially weak acidic solution increased slightly from 5.00 to 5.86 after 21 days, whereas the pH 3 solution increased to 4.57 over the same period. A more substantial change was observed

in the pH 1 group, where the solution pH rose from 1.00 to 2.95. The pH increase was most evident during the first 7 days, especially for the pH 1 and pH 3 groups, corresponding to the rapid mass loss at the same stage. After 14 days, the pH variation became less pronounced. Because the solutions were not buffered or renewed during exposure, the measured pH represents an evolving reaction environment rather than a constant acidity condition. The initial pH therefore defines the starting chemical boundary condition, while the subsequent pH increase reflects progressive acid consumption during fluid–rock interaction. This trend is consistent with the gradual consumption of easily reactive mineral surfaces and the possible accumulation of reaction products within local pore spaces. Therefore, the acid-induced alteration of shale should be treated as a time-dependent physicochemical process rather than a simple function of the initial pH.

The ion concentration results further clarify the chemical origin of the observed mass loss. As shown in Figure 1c, after 21 days of exposure, Ca^{2+} increased from 138 mg/L in the pH 5 group to 436 mg/L and 812 mg/L in the pH 3 and pH 1 groups, respectively. A similar but lower-magnitude increase was recorded for Mg^{2+}, which rose from 24 mg/L to 83 mg/L and 156 mg/L as the acidity increased. The enrichment of Ca^{2+} and Mg^{2+} is consistent with the dissolution of carbonate minerals, such as calcite and dolomite. In comparison, the concentrations of Al^{3+}, Fe^{3+}, K^{+}, Na^{+} and dissolved Si were much lower, but they also increased under stronger acidic conditions. For example, dissolved Si increased from 12.6 mg/L in the pH 5 group to 48.1 mg/L in the pH 1 group after 21 days. This ion-release pattern suggests that carbonate dissolution was probably the dominant contributor to early chemical mass loss, while clay minerals and aluminosilicate phases may also have participated in the prolonged acid–shale reaction. The latter process should be interpreted cautiously, because ion release alone cannot distinguish between mineral dissolution, ion exchange and the mobilization of loosely bound components.

Ultrasonic measurements reveal that the acid treatment also weakened the internal continuity of the shale skeleton. The initial P-wave velocity of the control samples was approximately 3020 m/s. After 21 days of acidic exposure, the velocity decreased to 2804 m/s in the pH 5 group, 2541 m/s in the pH 3 group and 2189 m/s in the pH 1 group, corresponding to velocity degradation rates of 7.2%, 15.9% and 27.5%, respectively. Compared with mass loss, the velocity response was more sensitive to internal deterioration, because wave propagation depends not only on mineral removal but also on grain contact, bedding interfaces and microcrack connectivity. The pronounced velocity reduction in the strongly acidic group therefore points to a loss of structural compactness within the shale matrix, rather than only surface-level corrosion.

To provide a unified descriptor for the subsequent creep analysis, the comprehensive acid-induced damage variable D_c was recalculated by integrating mass loss, P-wave velocity degradation, and porosity increase. As shown in Figure 1d, D_c increased from 0.052 to 0.081 and 0.114 in the pH 5 group after 7, 14, and 21 days, respectively. For the pH 3 group, the corresponding D_c values were 0.158, 0.218, and 0.274. The pH 1 group exhibited the highest damage levels, with D_c increasing from 0.286 after 7 days to 0.392 after 14 days and 0.499 after 21 days. The separation between the pH 3 and pH 1 groups remained evident with increasing exposure time, indicating that stronger acidity promoted progressively greater physicochemical deterioration. The separation between the pH 3 and pH 1 groups became evident after 14 days, suggesting that strong acidity continued to promote internal deterioration after the initial rapid reaction stage.

Because P-wave velocity degradation is one component used in the calculation of D_c, the two curves in Figure 1d should not be interpreted as independent validation of each other. Rather, their similar increasing trends reflect the contribution of internal structural deterioration to the overall acid-induced damage state. This distinction is important for the

following mechanical analysis. Initial pH and exposure time describe the external chemical environment, whereas D_c represents the actual damage state of the shale after acid treatment. For this reason, D_c is used in the subsequent sections to relate physicochemical alteration to creep strain accumulation, steady-state creep rate, long-term strength degradation and constitutive parameter evolution.

3.2. Mineral Dissolution and Multiscale Pore–Fracture Reconstruction

The XRD patterns provide the first evidence that acidic exposure selectively altered the mineral assemblage of the shale samples. As shown in Figure 2a, quartz-related reflections remained clearly identifiable after acid treatment, whereas the carbonate-related peaks, especially those assigned to calcite and dolomite, became progressively weaker as the initial pH decreased. The characteristic calcite peak near 29.4° and the dolomite-related reflection near 31.1° were still visible in the pH 5 for 21 d sample, but their relative intensities were markedly reduced in the pH 3 for 21 d and pH 1 for 21 d samples. Because the XRD patterns were vertically offset for clarity, the comparison focuses on relative peak changes within each pattern rather than the absolute intensity level between different curves. The attenuation of carbonate-related reflections corresponds well to the enrichment of Ca^{2+} and Mg^{2+} in the reacted solutions, supporting carbonate dissolution as a major mineralogical response during acidic exposure.

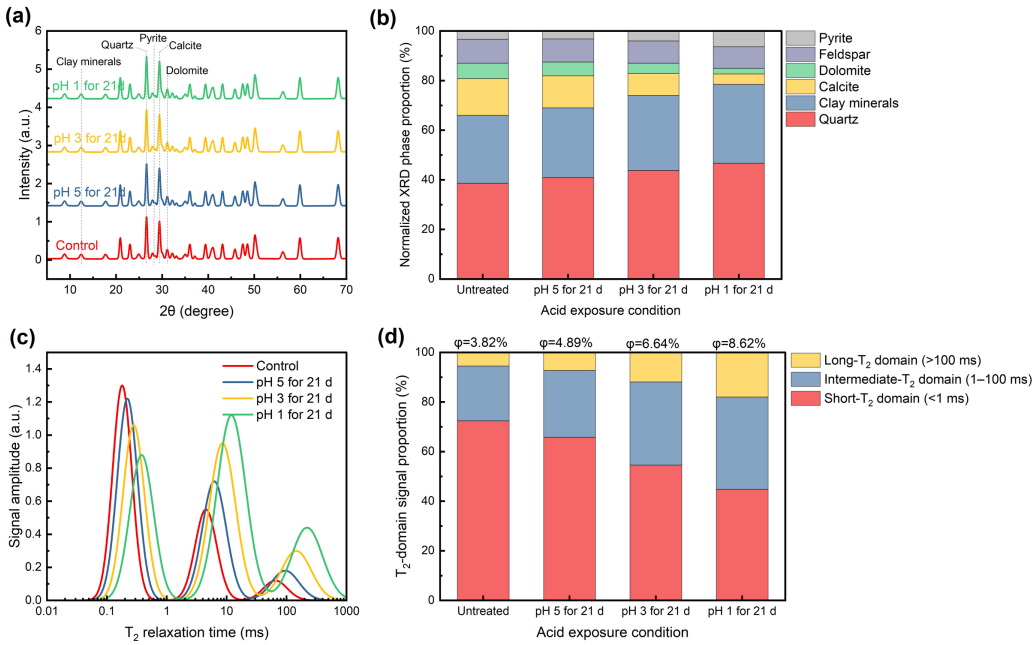


Figure 2. Mineral dissolution and pore–fracture reconstruction of shale after acidic exposure: (**a**) XRD patterns of control and acid-treated shale samples; (**b**) semi-quantitative normalized mineral proportions derived from XRD whole-pattern fitting; (**c**) NMR T_2 relaxation time distributions; and (**d**) relative signal proportions of the operational T_2 domains derived from NMR spectra.

The semi-quantitative normalized phase proportions derived from XRD further characterize the mineralogical response to acidic exposure. As presented in Figure 2b, the normalized calcite proportion decreased from 14.8% in the control shale to 12.9%, 8.9%, and 4.2% after 21 days of exposure at pH 5, pH 3, and pH 1, respectively. The normalized dolomite proportion showed a similar decrease, from 6.2% to 5.6%, 4.1%, and 2.3%. In contrast, the normalized proportions of quartz and clay minerals increased from 38.6% and 27.4% in the control sample to 46.7% and 31.8% in the pH 1 for 21 d sample, respectively. Importantly, these XRD percentages are normalized relative phase proportions

obtained from analyzed powder subsamples and should not be interpreted as absolute whole-specimen mineral mass fractions. Directly combining these normalized proportions with the measured 4.68% gravimetric mass loss would therefore not constitute a valid mineral mass balance. The gravimetric measurement provides the constraint on total material loss, whereas the XRD results are used to identify relative phase depletion or enrichment. Accordingly, the apparent increases in quartz, clay minerals, and pyrite reflect normalization after preferential alteration of acid-sensitive phases and may also contain contributions from subsample heterogeneity and semi-quantitative fitting uncertainty; they do not indicate formation of these minerals during acid exposure.

The NMR T_2 relaxation spectra show a pronounced redistribution of relaxation components after acidic exposure. In Figure 2c, the control shale is dominated by the short-T_2 component, whereas the relative contributions of the intermediate- and long-T_2 components progressively increase after acid treatment, particularly in the pH 3 for 21 d and pH 1 for 21 d groups. Importantly, this shift toward longer T_2 values cannot be attributed uniquely to pore enlargement because acid-induced mineral dissolution and surface-chemistry alteration may also modify the surface relaxivity. Therefore, the NMR results are interpreted here as evidence of a redistribution of water-associated relaxation environments rather than as a direct measurement of pore-size enlargement or pore connectivity. The structural opening and fracture development inferred from this relaxation redistribution are evaluated independently using the SEM and micro-CT observations described below.

The relative T_2-domain signal proportions further quantify the redistribution of the relaxation response. As shown in Figure 2d, the total NMR porosity increased from 3.82% in the control shale to 4.89%, 6.64%, and 8.62% in the pH 5 for 21 d, pH 3 for 21 d, and pH 1 for 21 d samples, respectively. Meanwhile, the short-T_2 ($<$1 ms) signal fraction decreased from 72.4% to 65.8%, 54.6%, and 44.8%. In contrast, the intermediate-T_2 (1–100 ms) fraction increased from 22.1% in the control shale to 37.2% in the pH 1 for 21 d sample, while the long-T_2 ($>$100 ms) fraction increased from 5.5% to 18.0%. Accordingly, the combined $T_2 > 1$ ms signal fraction increased from 27.6% to 55.2%, and the long-T_2 signal contribution increased by approximately 3.3 times. These values represent relaxation-domain signal fractions rather than geometric pore-size fractions, and they do not provide a direct measure of pore connectivity. The progressive redistribution toward longer T_2 components is nevertheless consistent with the independent SEM and micro-CT evidence of acid-induced structural opening and fracture development.

SEM–EDS observations provide direct local evidence for the micromorphological contrast between the control and strongly acid-treated end-member states. As shown in Figure 3a, the control shale exhibits a relatively compact matrix, with mineral particles closely bonded and only limited discontinuous microcracks along bedding-related weak planes. In contrast, the pH 1 for 21 d sample shows pronounced surface etching, enlarged dissolution pits, weakened cementing regions, and locally opened microcracks (Figure 3c). These observations indicate substantial local structural degradation after strong acidic exposure. The corresponding EDS spectra further characterize the elemental differences between the selected regions of the control and pH 1 for 21 d samples, as shown in Figure 3b,d.

EDS spectra from selected analysis areas further connect the micromorphological changes with carbonate-related mineral dissolution. Compared with the control shale, the pH 1 for 21 d sample shows a pronounced reduction in Ca and Mg peaks, while Si and Al become relatively enriched in the residual framework. This elemental change is consistent with the attenuation of carbonate-related XRD reflections, the decrease in the normalized calcite and dolomite proportions, and the increased Ca^{2+} and Mg^{2+} concentrations in the reacted solutions. The EDS evidence should be viewed as local rather than bulk quantifica-

tion, but it helps explain why the etched regions and weakened cement observed in SEM are closely associated with carbonate loss and residual aluminosilicate enrichment.

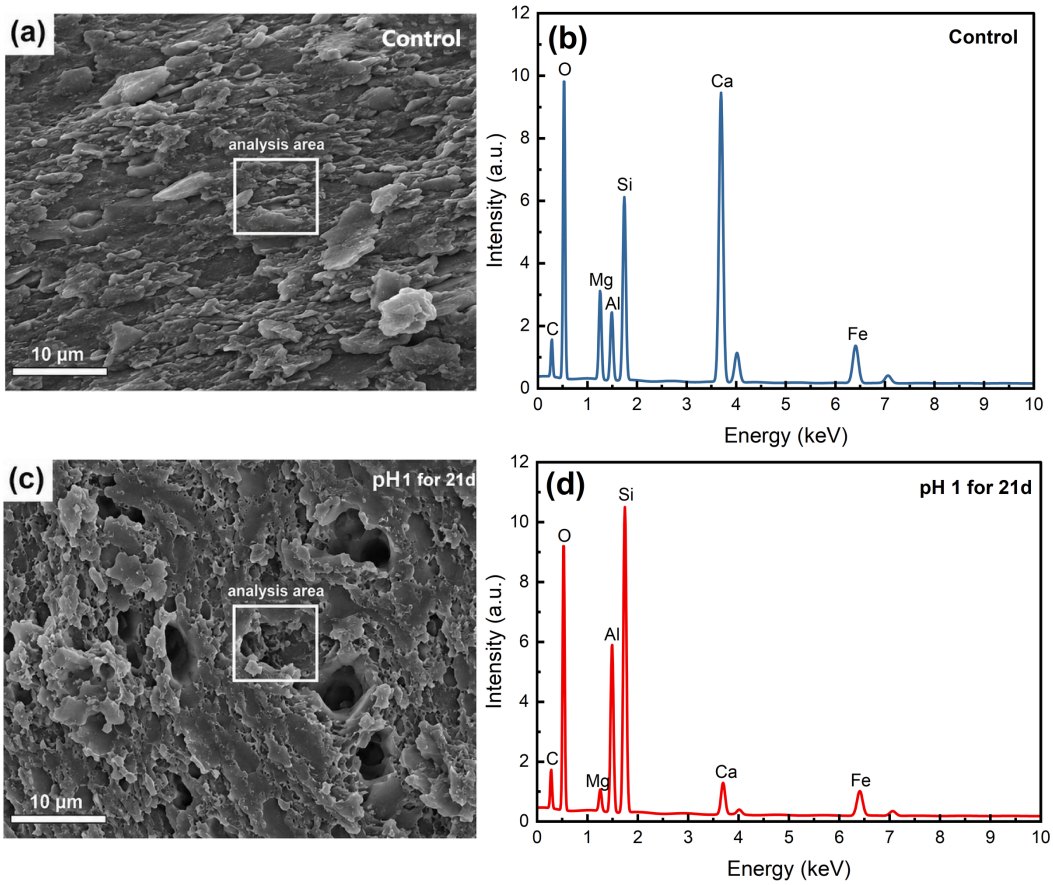


Figure 3. SEM–EDS characterization of the control and strongly acid-treated shale: (**a**) SEM image of the control sample; (**b**) EDS spectrum of the selected area in the control sample; (**c**) SEM image of the pH 1 for21 d sample; and (**d**) EDS spectrum of the selected area in the pH 1 for21 d sample.

Representative micro-CT images were used as an additional three-dimensional observation of fracture-network development between the two end-member states. As shown in Figure 4, the control shale contains only sparse and discontinuous fracture segments in the reconstructed volume, whereas the pH 1 for 21 d sample displays a more connected fracture network. Within the analyzed region of interest, the segmented fracture volume fraction increased from 0.19% in the control shale to 1.27% after pH 1 exposure, while the fraction of segmented fracture volume belonging to the largest connected cluster increased from 28.6% to 73.2%. These quantitative descriptors support the visual increase in resolvable fracture abundance and connectivity after strong acid treatment. This contrast is consistent with the NMR-observed redistribution toward longer T_2 components and with the reduction in P-wave velocity, while the micro-CT images provide the direct three-dimensional evidence for increased resolvable fracture development and connectivity. Because the micro-CT comparison was limited to the two end-member specimens and to features resolvable at the 5 μm voxel scale, the above values should be interpreted as quantitative descriptors of the selected reconstructed volumes rather than as population-scale estimates of total shale microfracture content.

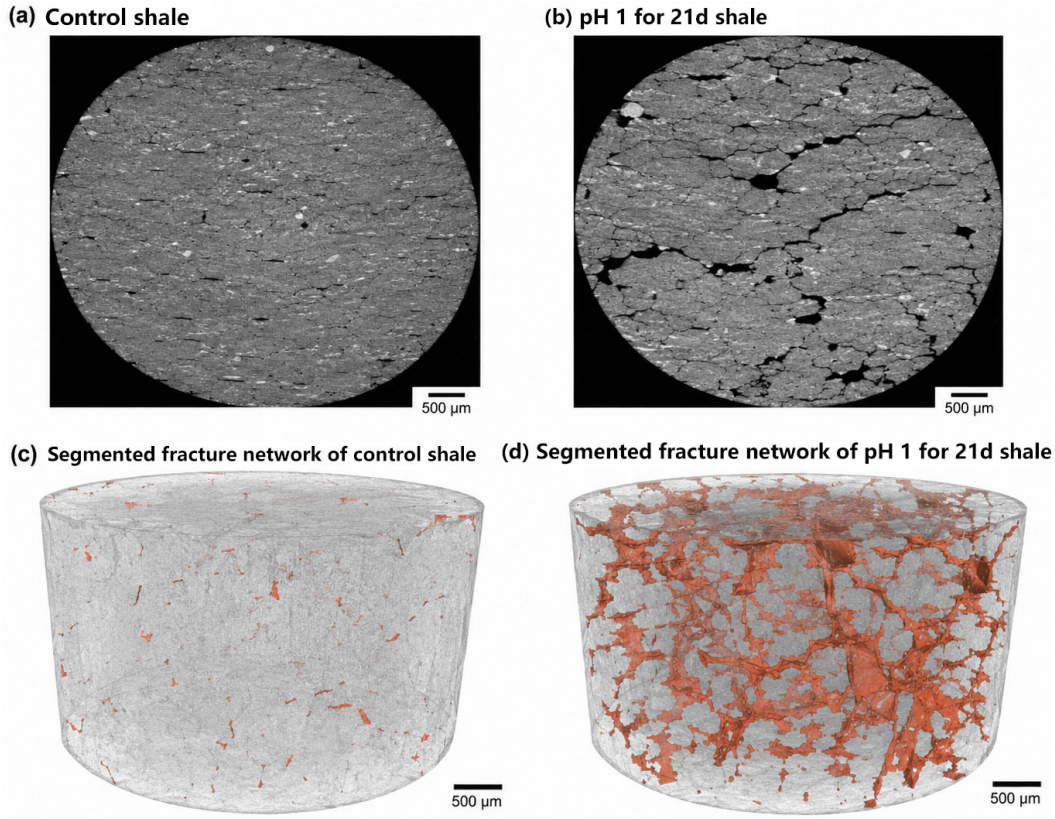


Figure 4. Representative micro-CT characterization of fracture-network development in the control and strongly acid-treated shale samples: (**a**,**b**) grayscale CT slices of control and pH 1 for 21 d samples; (**c**,**d**) segmented fracture networks reconstructed from the corresponding core volumes. The control and pH 1 for 21 d samples were selected as end-member states to show the three-dimensional contrast in fracture development after strong acidic exposure.

Taken together, the XRD, NMR, SEM–EDS and micro-CT observations point to a coupled mineralogical–structural deterioration process. Carbonate mineral dissolution provided a direct pathway for mass removal, while the weakening of carbonate-bearing cement reduced local bonding between mineral grains and bedding-related interfaces. As acidic exposure intensified, the NMR relaxation response shifted from the short-T_2 domain toward increased intermediate- and long-T_2 signal contributions, indicating a redistribution of water-associated relaxation environments. The micro-CT comparison between the two end-member samples further supports the development of a more connected fracture network under strong acid treatment. This multiscale pore–fracture reconstruction and associated structural degradation provide a plausible basis for the subsequent creep response: a shale matrix with reduced cementation, higher porosity, more open grain boundaries, and greater micro-CT-resolved fracture connectivity is expected to exhibit lower resistance to time-dependent deformation. Accordingly, mineral dissolution, NMR relaxation redistribution, SEM-observed etching, and micro-CT-resolved fracture development are treated here as measured structural evidence, whereas the subsequent stress concentration, interface sliding, and damage-accelerated deformation discussed in Section 3.6 represent mechanistic interpretations derived from the combined experimental observations rather than quantities measured directly.

3.3. Creep Strain–Time Behavior Under Different Acid-Induced Damage Levels

Figure 5a shows the mean axial creep strain–time responses of three independent shale specimens for each acid-induced damage level under stepwise differential loading,

with the corresponding SD represented by shaded uncertainty bands. Each loading stage produced an immediate strain jump, followed by a time-dependent deformation segment under constant stress. The control group showed the lowest strain accumulation throughout the test, with a mean cumulative axial strain of 0.687% after 24 h. The pH 5 for 21 d group followed a similar curve shape but reached a higher mean final strain of 0.958%, suggesting that weak acidic exposure had already increased the deformability of the shale matrix, although the creep process remained relatively stable.

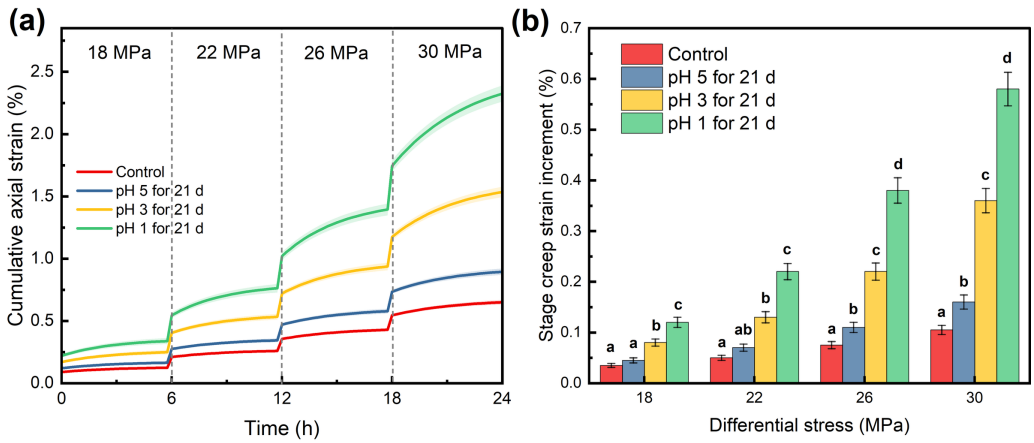


Figure 5. Creep strain–time behavior of shale under different acid-induced damage levels: (**a**) cumulative axial strain–time responses under stepwise differential loading, shown as the pointwise mean of three independent specimens with shaded bands representing ±1 SD; (**b**) stage creep strain increments at different differential stress levels, presented as mean ± SD ($n = 3$). For panel (**b**), differences among the control and acid-treated groups were evaluated separately at each differential stress level using one-way ANOVA followed by Tukey's HSD post hoc test. Different lowercase letters indicate significant differences among groups at the same stress level ($p < 0.05$).

The influence of acid-induced damage became more evident at higher stress levels. For the pH 3 for 21 d group, the mean final cumulative axial strain increased to 1.620%, approximately 2.36 times the control mean. The curve separation was limited during the first loading stage at 18 MPa but became clearer after the differential stress increased to 26 MPa and 30 MPa. This trend suggests that acid-induced damage did not merely increase the initial compliance of shale; it also made the subsequent creep response more sensitive to stress level. Such behavior is consistent with the pore-structure redistribution described in Section 3.2, especially the decrease in small-pore proportion and the increase in medium to large pore spaces after stronger acidic exposure.

The pH 1 for 21 d group exhibited the most pronounced time-dependent deformation, with a mean cumulative axial strain of 2.480% at the end of the test, and the last loading stage did not approach a clear strain plateau. The strain continued to rise during the final hours at 30 MPa, pointing to an early tendency toward accelerated creep. This response is likely related to the higher damage variable D_c, stronger carbonate dissolution and larger pore–fracture proportion in the strongly acid-treated sample. Still, the curve itself cannot isolate a single controlling mechanism; it mainly shows that strong acidic exposure substantially reduced the resistance of shale to sustained deformation under high stress.

The stage creep strain increments in Figure 5b further quantify this difference. At 18 MPa, the mean creep strain increment increased from 0.035% in the control group to 0.052%, 0.080% and 0.120% in the pH 5 for 21 d, pH 3 for 21 d and pH 1 for 21 d groups, respectively. At 30 MPa, the corresponding values increased to 0.105%, 0.165%, 0.360% and 0.580%. At 18 MPa, the difference between the control and pH 5 for 21 d groups was not statistically significant ($p > 0.05$), whereas the more strongly acid-treated groups

showed significant increases. As the differential stress increased, the statistical separation among the treatment groups became progressively clearer, consistent with the stronger amplification of creep deformation at higher stress levels. The increase was therefore much sharper at higher stress, particularly for the pH 3 for 21 d and pH 1 for 21 d groups. This stress-dependent amplification is important for long-term stability evaluation, because chemically damaged shale may show only moderate deformation at low stress but become much more creep-sensitive once the stress approaches a critical level.

The separation between instantaneous strain and creep strain also deserves attention. The total instantaneous strain increased from 0.420% in the control shale to 1.180% in the pH 1-21 d sample, while the accumulated creep strain increased from 0.267% to 1.300%. The larger relative increase in the creep component suggests that acid treatment affected not only the short-term stiffness of shale, but also its delayed deformation capacity. This provides the basis for the following analysis of late-stage creep rate and the estimated long-term strength degradation.

3.4. Late-Stage Creep Rate and Estimated Long-Term Strength Threshold

The late-stage creep rate was evaluated over the final 2 h of each constant-stress stage according to the stability criteria defined in Section 2.8. The criteria were satisfied for the control, pH 5 for 21 d, and pH 3 for 21 d groups over the analyzed stress stages, whereas the pH 1 for 21 d group at 30 MPa showed a statistically significant increase in creep rate with time and was therefore characterized by an apparent late-stage creep rate rather than a quasi-steady rate. As shown in Figure 6a, the rate increased with differential stress for all samples, but the increase was much stronger after acidic exposure. For the control shale, the late-stage creep rate increased from 0.48×10^{-4} h^{-1} at 18 MPa to 1.55×10^{-4} h^{-1} at 30 MPa. After weak acidic treatment, the pH 5-21 d sample showed a slightly higher rate, reaching 2.35×10^{-4} h^{-1} at 30 MPa. The difference remained moderate, suggesting that weak acid exposure mainly increased deformability without changing the creep pattern substantially.

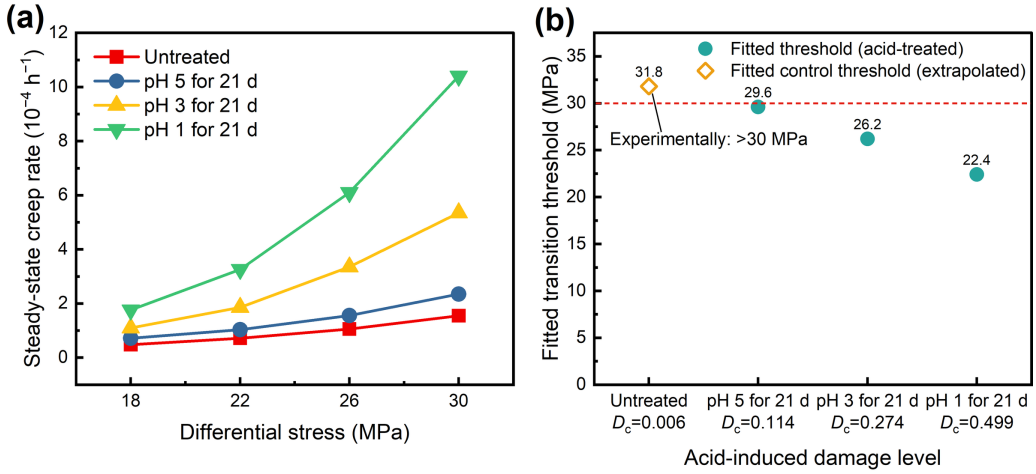


Figure 6. Late-stage creep rate and continuously fitted long-term strength thresholds under different acid-induced damage levels: (**a**) late-stage creep rate as a function of differential stress; (**b**) continuously fitted long-term strength thresholds under different acid-induced damage levels, with the corresponding damage variable D_c labeled for each group. Late-stage creep-rate data are presented as mean ± SD ($n = 3$). In panel (**b**), the open symbol represents the extrapolated fitted threshold of 31.8 MPa for the control group, whereas the filled symbols represent the fitted thresholds for the acid-treated groups. The experimentally constrained control threshold is >30 MPa, and the horizontal dashed line indicates the maximum applied differential stress of 30 MPa. For panel (**a**), differences among treatment groups were evaluated separately at each differential stress level using one-way ANOVA followed by Tukey's HSD post hoc test.

A sharper rate increase appeared in the more strongly damaged samples. At 30 MPa, the steady-state creep rate increased to 5.35×10^{-4} h^{-1} for the pH 3 for 21 d sample and the apparent late-stage creep rate reached 10.40×10^{-4} h^{-1} for the pH 1 for 21 d sample. The rate difference between the pH 3 for 21 d and pH 1 for21 d samples was relatively small at 18 MPa but expanded rapidly at higher stress. This stress-dependent response agrees with the strain–time curves in Figure 5a, where strong acid-induced damage became most evident during the final loading stage. According to the criterion defined in Section 2.9, only the pH 1 for 21 d group at 30 MPa exhibited a statistically significant positive temporal trend in creep rate ($p < 0.05$). This response is therefore interpreted as an early accelerated-creep tendency rather than as fully developed tertiary creep. It also suggests that acid-induced damage did not act as a fixed weakening coefficient; its influence became amplified when the applied stress approached the long-term stability limit.

The estimated long-term strength threshold obtained from the isochronous stress–strain response and late-stage creep-rate transition showed a systematic decrease with increasing acid-induced damage. Figure 6b presents the continuously fitted transition thresholds. The fitted control value of 31.8 MPa is an extrapolated constitutive-model parameter rather than a directly measured long-term strength, because no transition was observed within the maximum applied differential stress of 30 MPa; accordingly, the experimentally constrained control threshold remains >30 MPa. For the acid-treated groups, the experimentally constrained thresholds are reported as approximately 30 MPa for the pH 5 for 21 d group, 26 MPa for the pH 3 for 21 d group, and 22 MPa for the pH 1 for 21 d group. These values are reported to the nearest 1 MPa because the applied stress increment was 4 MPa and finer experimental resolution is not warranted. The corresponding continuous fitted values of 29.6, 26.2, and 22.4 MPa are plotted in Figure 6b and used for constitutive-model calibration. Relative to the fitted control threshold, the fitted threshold for the pH 1 for 21 d group decreased by 29.6% according to Equation (3); this reduction is model-derived and does not represent a directly measured experimental degradation ratio. The limited separation between the control and pH 5-21 d conditions contrasts with the progressively lower thresholds after stronger acid treatment, indicating a reduction in sustained load-bearing capacity with increasing acid-induced damage. Because the creep tests were limited to 24 h, these thresholds should be interpreted as duration-dependent transition estimates rather than intrinsic long-term strength constants.

The relation between D_c and long-term strength provides a state-based description that complements the nominal pH condition. Therefore, D_c was labeled together with each damage group in Figure 6b to emphasize that the evolution of the estimated threshold reflects the post-treatment damage state rather than only the nominal acidity of the solution. The pH value represents the external acidic condition, whereas D_c reflects the post-reaction physicochemical damage state after acid–shale interaction. When D_c increased from 0.006 in the control group to 0.499 in the pH 1 for 21 d group, the experimentally constrained long-term strength threshold shifted from >30 MPa to approximately 22 MPa. This trend supports the use of D_c as a state variable in the subsequent constitutive modeling. In practical terms, short-term strength parameters may underestimate deformation risk after strong acidic exposure because chemically damaged shale can approach nonlinear time-dependent deformation at progressively lower sustained stress levels.

3.5. Evolution and Performance of the Damage-Coupled Creep Constitutive Model

Based on the damage-coupled constitutive model defined in Section 2.11, the fitted parameters were analyzed to determine how acid-induced damage modified the viscoelastic response, long-term strength threshold and nonlinear creep tendency of shale.

The evolution of the normalized constitutive parameters is shown in Figure 7a and summarized quantitatively in Table 3. As D_c increased, the elastic moduli, viscosity coefficients and long-term strength threshold all decreased, but their sensitivities were different. The normalized instantaneous modulus $E_1/E_{1,u}$ decreased from 1.000 in the control shale to 0.458 in the pH 1 for 21 d sample, while $E_2/E_{2,u}$ decreased to 0.326. The viscosity-related parameters declined more strongly: $\eta_1/\eta_{1,u}$ and $\eta_2/\eta_{2,u}$ reached 0.149 and 0.241, respectively, at the highest damage level. In comparison, $\sigma_\infty/\sigma_{\infty,u}$ decreased more gradually, from 1.000 to 0.704. The effective damage sensitivity coefficients derived from the control and highest-damage endpoints were 1.584, 2.274, 3.862, 2.886, and 0.712 for E_1, E_2, η_1, η_2, and σ_∞, respectively. The normalized parameter values at intermediate damage levels were calculated using the exponential relationships in Equation (8), providing a consistent description of damage-dependent parameter evolution. This parameter sequence is consistent with the experimental observation that acid treatment caused a stronger increase in creep deformation than in instantaneous deformation. Because elastic-modulus degradation is excluded from the revised definition of D_c, the observed evolution of E1 and E2 with increasing D_c is not mathematically embedded in the damage variable. The stiffness parameters can therefore be evaluated as independent mechanical responses associated with the post-reaction physicochemical damage state.

The inclusion of $\sigma_\infty(D_c)$ is important for distinguishing ordinary creep enhancement from the onset of accelerated deformation. The decrease in long-term strength shifts the activation threshold of the viscoplastic term to a lower stress level. As a result, the strongly damaged pH 1 for 21 d sample entered a more nonlinear creep regime during the final loading stage, whereas the control and weakly damaged samples remained mainly within the viscoelastic or quasi-steady creep range under the same stress path. This treatment allows the model to account for the stress-threshold effect observed in the creep tests, instead of only fitting the curve shape through viscosity reduction.

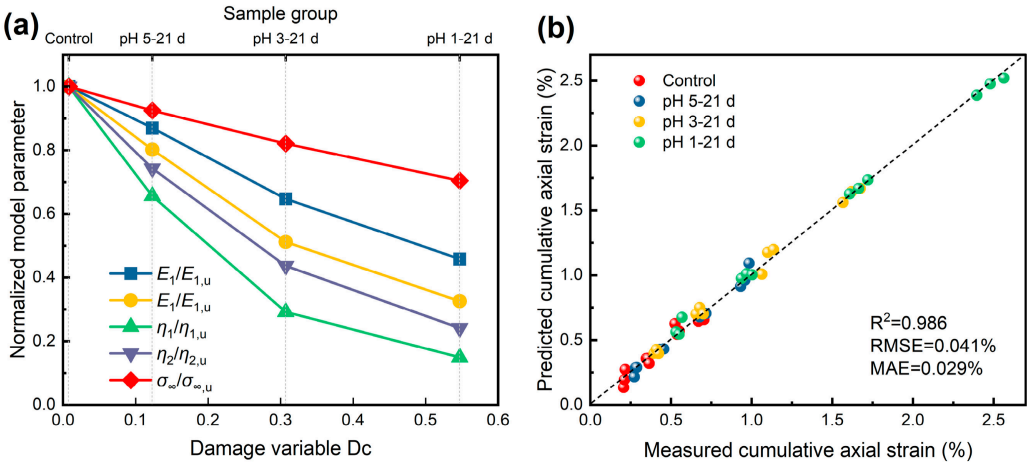


Figure 7. Parameter evolution and cross-validated performance of the damage-coupled creep constitutive model: (**a**) normalized viscoelastic parameters and long-term strength threshold as functions of the acid-induced damage variable D_c, with the corresponding sample groups labeled on the top axis; (**b**) comparison between the measured and predicted cumulative axial strains across the four treatment groups. The 1:1 line represents perfect agreement between the measured and predicted strain. The cross-validation performance metrics are summarized in Table 4. The parameters in (**a**) were normalized by the corresponding values of the control shale.

Model performance was evaluated by comparing the measured cumulative axial strain with the corresponding predictions of the damage-coupled formulation. The predicted cumulative strain curves were generated continuously over the complete 24-h loading path, with the material state at the end of each 6-h stage carried directly into the subsequent stage; no strain component was reinitialized at the stress boundaries. Figure 7b presents a comparison between the measured and predicted cumulative axial strains, with the dashed 1:1 line indicating perfect agreement. The plotted points illustrate the agreement pattern across the four treatment groups, while the quantitative cross-validation results are reported separately in Table 3. The threefold specimen-level cross-validation yielded a pooled R^2 of 0.986, RMSE of 0.041%, and MAE of 0.029%, indicating that the model retained good predictive performance for specimens not used in parameter calibration. Under the same cross-validation partitions, the conventional Burgers model yielded $R^2 = 0.958$, RMSE = 0.070%, and MAE = 0.051%. The conventional Nishihara model showed intermediate predictive performance, with $R^2 = 0.972$, RMSE = 0.056%, and MAE = 0.039%. In comparison, the proposed damage-coupled model achieved $R^2 = 0.986$, RMSE = 0.041%, and MAE = 0.029%. The cross-validation performance of the three constitutive models is summarized in Table 3. Relative to the Burgers model, the proposed formulation reduced RMSE and MAE by 41.4% and 43.1%, respectively; relative to the Nishihara model, the corresponding reductions were 26.8% and 25.6%. The advantage became most apparent for the strongly damaged pH 1 for 21 d specimens at the highest stress level, where the conventional Burgers model lacks a yield-controlled viscoplastic response and the classical Nishihara model does not account for the continuous evolution of creep parameters with the independently measured physicochemical damage state. The larger Burgers-model deviations occurred mainly for the strongly damaged shale at the highest stress level, where the damage-dependent strength threshold and nonlinear deformation term included in the proposed model became increasingly relevant. Bootstrap analysis showed finite parameter uncertainty, with relative 95% confidence-interval widths of 8.1–19.3%. The maximum absolute bootstrap correlation between fitted parameters was 0.84, while ±10% individual parameter perturbations changed the validation RMSE by 5.6–20.8%, indicating that no fitted parameter was effectively redundant within the tested range. These aggregate uncertainty and sensitivity diagnostics are also summarized in the note to Table 3, providing complementary information on parameter stability without assigning the overall uncertainty ranges to individual treatment groups. Slightly larger deviations were still observed for the pH 1 for 21 d group at high strain levels, which may reflect increasingly localized damage and fracture interaction as the sample approaches the accelerated-creep regime, whereas the present formulation treats the shale as a homogenized continuum.

Table 3. Damage-dependent normalized constitutive parameters and model uncertainty diagnostics.

Parameter	Control ($D_c = 0.006$)	pH 5 for 21 d ($D_c = 0.114$)	pH 3 for 21 d ($D_c = 0.274$)	pH 1 for 21 d ($D_c = 0.499$)	Sensitivity Coefficient λ
$E_1/E_{1,u}$	1.000	0.843	0.654	0.458	1.584
$E_2/E_{2,u}$	1.000	0.782	0.544	0.326	2.274
$\eta_1/\eta_{1,u}$	1.000	0.659	0.355	0.149	3.862
$\eta_2/\eta_{2,u}$	1.000	0.732	0.461	0.241	2.886
$\sigma_\infty/\sigma_{\infty,u}$	1.000	0.926	0.826	0.704	0.712

Note: The intermediate normalized parameter values were calculated using Equation (8), with effective damage sensitivity coefficients derived from the control and pH 1 for 21 d endpoints. The reported model-level uncertainty diagnostics include relative bootstrap 95% confidence-interval widths of 8.1–19.3%, a maximum absolute parameter correlation of 0.84, and validation RMSE variations of 5.6–20.8% under ±10% parameter perturbations.

Table 4. Cross-validation performance of different creep constitutive models.

Model	R^2	RMSE/%	MAE/%
Conventional Burgers	0.958	0.070	0.051
Conventional Nishihara	0.972	0.056	0.039
Proposed damage-coupled model	0.986	0.041	0.029

As summarized in Table 4, introducing a yield-dependent viscoplastic component improved the prediction relative to the Burgers model, while further coupling the constitutive parameters to the independently characterized physicochemical damage state provided additional improvement over the conventional Nishihara formulation.

The proposed model should therefore be understood as an experimentally calibrated constitutive description within the tested damage and stress ranges. Its value lies in converting the acid-induced damage state into mechanical parameters that control stiffness, viscous resistance, and long-term strength. Compared with a conventional Burgers model evaluated under the same specimen-level cross-validation framework, the damage-coupled formulation provided lower prediction errors and a continuous link among mineral dissolution, pore–fracture reconstruction, long-term strength loss, and creep parameter evolution. Further external validation under longer creep durations, different bedding orientations, and coupled temperature–fluid conditions is still required before the model can be extended to field-scale prediction.

3.6. Mechanistic Link Between Pore–Fracture Reconstruction and Damage-Dependent Creep Evolution

The results above show that the creep enhancement of acid-treated shale is not governed by a single factor such as mass loss or initial pH alone. Instead, it reflects a coupled response involving carbonate dissolution, cement weakening, pore–fracture reconstruction, and the degradation of time-dependent mechanical resistance. In this framework, the initial pH defines the external chemical condition, whereas the damage variable D_c characterizes the internal damage state actually reached after acid–shale interaction. This distinction is important because samples exposed to different acidic environments did not simply experience different degrees of corrosion; they developed different internal structures, which subsequently influenced strain accumulation under sustained stress. Figure 8 therefore summarizes an experimentally supported structural-evolution pathway together with the proposed mechanical mechanisms linking pore–fracture reconstruction to damage-dependent creep.

The first step in this process is the preferential dissolution of acid-sensitive mineral components. The increase in Ca^{2+} and Mg^{2+} concentrations, together with the progressive attenuation of calcite- and dolomite-related XRD reflections, indicates that carbonate dissolution is the dominant chemical pathway during acidic exposure. Because carbonate minerals and carbonate-bearing cement contribute to interparticle bonding in shale, their dissolution weakens grain contacts and bedding-related interfaces. The apparent relative increases in quartz, clay minerals, and pyrite should therefore be interpreted as normalized XRD enrichment consistent with preferential carbonate alteration, potentially influenced by powder-subsample heterogeneity and semi-quantitative fitting uncertainty, rather than as evidence for the formation of new minerals. This preferential carbonate alteration provides a mineralogical basis for the subsequent structural deterioration.

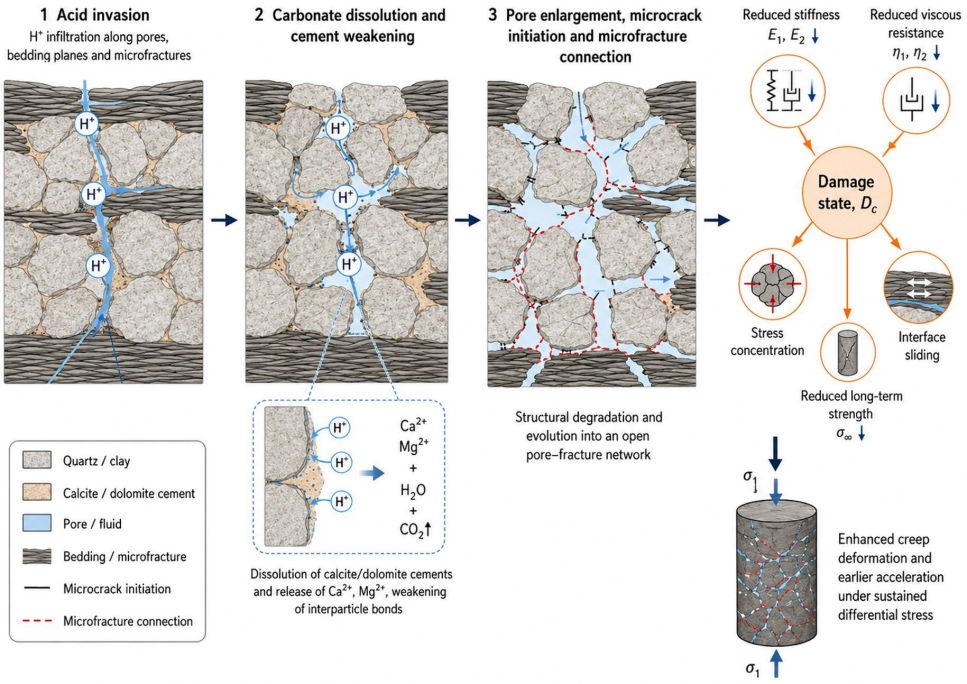


Figure 8. Conceptual pathway linking experimentally observed acid-induced mineralogical and pore–fracture changes to damage-dependent creep evolution in shale. Carbonate dissolution, cement weakening, pore redistribution, fracture development, and creep enhancement are supported by the present experimental observations, whereas stress concentration, interface sliding, and microcrack interaction represent proposed mechanical mechanisms inferred from the combined structural and creep responses. Blue arrows within pores indicate acid/fluid transport, dark-blue arrows show pathway progression, and orange arrows indicate proposed mechanical links. The blue dashed callout marks the magnified dissolution site; inward red and opposed white arrows indicate stress concentration and interface sliding, respectively.Downward arrows beside model parameters indicate decreases.

The structural response becomes clearer when the multiscale pore–fracture evidence is considered together. The NMR T_2 spectra shifted toward longer relaxation times, with increasing relative contributions from the intermediate- and long-T_2 domains as acid-induced damage increased. Because surface relaxivity may also change during acid treatment, this relaxation redistribution is not interpreted independently as a quantitative change in pore size or connectivity. SEM observations further showed the development of etched pores, partial opening of grain boundaries and weakening of cement bridges, while EDS spectra revealed local depletion of Ca and Mg and relative enrichment of Si and Al in the residual framework. The representative micro-CT comparison between the control and pH 1 for 21 d samples also showed that strong acidic exposure promoted a more connected internal fracture network. Together with the reduction in P-wave velocity, these results support the view that acid treatment transformed the shale from a relatively compact matrix into a more heterogeneous and more compliant pore–fracture system.

This structural degradation provides a plausible basis for the observed increase in stress sensitivity of the creep response. At low differential stress, the control and weakly acid-treated samples still showed limited separation in creep strain, suggesting that the remaining solid framework could still sustain the applied load with moderate time-dependent deformation. As stress increased, the damaged samples, especially the pH 3 for 21 d and pH 1 for 21 d groups, showed a sharper increase in cumulative strain and steady-state creep rate. This transition is consistent with a reduced resistance of weakened grain contacts and bedding interfaces to delayed deformation and may also reflect enhanced local stress concentration around enlarged pores and connected microfractures. In the pH 1 for 21 d sample, the final loading stage already showed an early tendency toward accelerated

creep, which is consistent with, but does not directly demonstrate, increasing deformation localization and microcrack interaction at the highest damage and stress levels.

The constitutive parameters provide a mechanical expression of this damage pathway. The reductions in E_1 and E_2 reflect the loss of elastic stiffness after acid treatment, whereas the larger reductions in η_1 and η_2 indicate weakened resistance to sustained deformation. In addition, the decrease in the long-term strength threshold σ_∞ means that the stress level required to activate a more nonlinear creep response becomes lower as acid-induced damage increases. This explains why the strongly damaged shale not only accumulated larger creep strain, but also showed an earlier transition toward accelerated deformation under the same loading path. In this sense, acid-induced chemical damage did not merely soften the shale at the moment of loading; it also reduced both the viscous stabilization capacity and the long-term load-bearing threshold of the material.

Based on these observations, the mechanistic pathway from acid-induced structural reconstruction to damage-dependent creep evolution can be summarized as follows: acidic fluid first invades pores, bedding planes and pre-existing microfractures, where it preferentially dissolves carbonate minerals and weakens cementing components; the weakened framework then promotes pore enlargement, microcrack initiation and partial pore–fracture connection; this multiscale structural degradation reduces elastic stiffness, viscous resistance and long-term strength; under sustained differential stress, the resulting heterogeneous structure is proposed to promote local stress concentration and interface sliding, providing a plausible mechanical pathway for the larger creep strain and higher creep rate observed in the damaged shale. At sufficiently high damage and stress levels, interaction among weakened interfaces and microcracks may further contribute to the observed early accelerated-creep tendency. This mechanism links the physicochemical damage variable D_c with the observed strain evolution, long-term strength degradation and parameter decay in the damage-coupled creep constitutive model.

3.7. Engineering Implications and Limitations

The present results have practical implications for shale formations exposed to acidic or other reactive fluids during drilling, stimulation, and production. A central finding is that the nominal acidity of the fluid alone does not fully characterize the resulting mechanical state of shale. Samples subjected to different acidic conditions developed distinct post-reaction damage states, and the subsequent creep response can be interpreted more consistently in terms of the integrated damage variable D_c, which incorporates mass loss, P-wave velocity degradation, and porosity increase. For engineering assessment, these post-reaction physicochemical and mechanical changes should therefore be considered together when evaluating acid-induced weakening, rather than representing the effect solely by the initial fluid pH. The present results are most appropriately interpreted as a controlled mechanistic baseline for chemically induced shale degradation. They demonstrate how acid-driven mineral dissolution and pore–fracture reconstruction can modify subsequent time-dependent deformation, but the measured damage levels and creep parameters should not be transferred directly to reservoir conditions without formation-specific calibration.

For wellbore stability, the results indicate that chemically altered shale can become increasingly susceptible to sustained deformation as both damage level and differential stress increase. The control shale exhibited limited creep accumulation under the tested loading path, whereas the strongly acid-treated sample developed substantially greater cumulative strain and showed an early tendency toward accelerated creep at the highest stress level. Such behavior suggests that assessments based only on instantaneous or short-duration mechanical responses may underestimate the potential for delayed deformation after strong fluid–rock interaction. The decrease in the damage-dependent long-term strength threshold

$\sigma_\infty(D_c)$ further indicates that chemically weakened shale may approach nonlinear creep behavior at lower sustained stress levels.

The results also have implications for mechanically loaded shale surrounding stimulated fractures. Acidic exposure increased pore volume and promoted the development of larger and more connected pore–fracture domains, but these structural changes were accompanied by reductions in elastic stiffness, viscous resistance, and long-term strength. The experimentally constrained long-term strength threshold decreased from >30 MPa in the control shale to approximately 22 MPa in the pH 1 for 21 d sample. Thus, acid-induced enhancement of pore–fracture connectivity may occur simultaneously with deterioration of the long-term load-bearing capacity of the surrounding shale matrix. Acid strength and exposure duration should therefore be evaluated not only in terms of mineral reactivity and pore development, but also with respect to their potential influence on long-term mechanical stability under sustained stress.

The damage-coupled constitutive formulation provides a quantitative framework for translating the post-reaction damage state into parameters governing stiffness, viscous resistance, and the long-term strength threshold. By introducing D_c into E_1, E_2, η_1, η_2, and σ_∞, the formulation links experimentally measurable physicochemical deterioration with the observed time-dependent mechanical response. Within the tested stress and damage ranges, this framework can provide a basis for updating creep parameters after fluid–rock interaction. Its extension to field-scale applications, however, requires calibration and independent validation using formation-specific mineralogical, petrophysical, mechanical, and fluid-condition data.

Several limitations should be recognized. First, the present experiments used static HCl exposure at 25 ± 1 °C as a controlled chemical condition and therefore do not reproduce the full complexity of reservoir fluid–rock interaction. Actual formation brines, CO_2-bearing fluids, flowback fluids, and stimulation fluids may contain high ionic strength, multivalent ions, dissolved gases, and chemical additives that can modify mineral dissolution, ion exchange, secondary precipitation, and clay-related reactions. In addition, the present batch system was not renewed during exposure, so acid was progressively consumed and reaction products accumulated in the solution. Under field-scale flow-through conditions, continuous fluid transport may instead replenish reactive species and remove dissolved products and mobilized fines, thereby changing both the reaction extent and its spatial distribution. Reservoir temperature, pore pressure, confining stress, and fluid-flow rate may further influence reaction kinetics, transport pathways, fracture aperture, and chemo-mechanical coupling. Second, creep testing was performed on dried specimens after acid treatment to isolate irreversible chemical damage. Consequently, the present results do not include the coupled effects of retained pore fluids, pore pressure, capillary forces, or ongoing fluid–rock reactions during sustained loading. Third, the creep tests were conducted over a limited duration and stress range. Longer-duration experiments are required to determine whether the observed accelerated tendency develops into complete tertiary creep or failure. Fourth, all specimens were prepared with their axes normal to the bedding plane ($\theta = 90°$) and tested under this fixed orientation to reduce anisotropy-induced variability and isolate the influence of acid-induced damage. The present results therefore represent a controlled bedding configuration rather than a bedding-independent material response; different bedding orientations, lamination densities, and mineralogical heterogeneity may alter acid penetration, crack evolution, and time-dependent deformation and require further systematic investigation. Accordingly, the reported long-term strength values should be regarded as test-duration-dependent threshold estimates, and the control threshold remains constrained only as being greater than 30 MPa under the present loading protocol.

The microstructural characterization also has scale-dependent limitations. SEM–EDS provides direct local evidence of etched pores, cement weakening, and elemental redistribution, but represents selected regions rather than the entire specimen volume. Micro-CT provides three-dimensional visualization of fracture-network differences between the control and strongly acid-treated end-member samples, but does not quantify the complete evolution across all damage levels. Its spatial resolution also limits the identification of finer pore domains. Accordingly, D_c should be regarded as an integrated state descriptor constructed from complementary measurements rather than as a direct measurement obtained from a single characterization technique.

Finally, the proposed constitutive formulation remains an experimentally calibrated continuum description. It captures the observed damage-dependent degradation of creep-related parameters within the tested range but does not explicitly resolve local crack coalescence, mineral-scale heterogeneity, or bedding-interface slip. Extrapolation beyond the experimental conditions therefore requires further verification under longer creep durations, saturated or continuously reactive conditions, different bedding orientations, true triaxial stress states, and more realistic fluid chemistries.

4. Conclusions

The coupled mineralogical, structural, and time-dependent mechanical evolution of shale subjected to acidic exposure was investigated through multiscale characterization, stepwise triaxial creep testing, and damage-dependent constitutive analysis. The main conclusions are as follows:

(1) Acid–shale interaction promoted preferential dissolution of carbonate minerals and progressive reconstruction of the pore–fracture system. The attenuation of calcite- and dolomite-related XRD reflections and the decrease in their normalized XRD proportions, together with the increased Ca^{2+} and Mg^{2+} concentrations in the reacted solutions, indicate that carbonate dissolution was the dominant chemical pathway under the tested acidic conditions. As acid-induced deterioration intensified, the total NMR porosity increased from 3.82% to 8.62%, while the long-T_2 (>100 ms) signal fraction increased from 5.5% to 18.0%. Combined NMR, SEM–EDS, micro-CT, and P-wave velocity results indicate that the shale evolved from a relatively compact matrix toward a more heterogeneous and interconnected pore–fracture structure.

(2) Increasing post-reaction damage was accompanied by a pronounced enhancement in the time-dependent deformation response. The final cumulative axial strain increased from 0.687% in the control shale to 2.480% in the pH 1 for 21 d sample, while the late-stage creep rate at 30 MPa increased from 1.55×10^{-4} h^{-1} in the control group to an apparent late-stage rate of 10.40×10^{-4} h^{-1} in the pH 1-21 d group. Meanwhile, the estimated long-term strength threshold decreased from >30 MPa in the control group to approximately 22 MPa in the pH 1 for 21 d group. The amplification of creep response became more pronounced at higher differential stress, indicating that strongly acid-damaged shale is increasingly susceptible to sustained deformation as the applied stress approaches its long-term stability limit.

(3) The comprehensive damage variable D_c, constructed from mass loss, P-wave velocity degradation, and porosity increase, provides a dimensionless descriptor of the relative post-reaction damage state within the tested conditions. Incorporating D_c into the viscoelastic–viscoplastic formulation enabled the damage-dependent degradation of elastic stiffness, viscous resistance, and long-term strength threshold to be represented within a unified framework. At the highest damage level, $E_1/E_{1,u}$, $E_2/E_{2,u}$, $\eta_1/\eta_{1,u}$, $\eta_2/\eta_{2,u}$, and $\sigma_\infty/\sigma_{\infty,u}$ decreased to 0.458, 0.326, 0.149, 0.241, and 0.704, respectively. Within the tested stress and damage ranges, the formulation reproduced the overall

creep response with low prediction errors, demonstrating its ability to quantitatively describe the evolution of creep-related mechanical parameters with increasing acid-induced damage.

Overall, the principal contribution of this study is not the identification of preferential carbonate dissolution itself, but the quantitative linkage of the independently characterized post-reaction physicochemical damage state with history-dependent creep deformation, strength-threshold evolution, and constitutive parameters within a unified and cross-validated framework. The framework provides a quantitative basis for assessing the long-term mechanical response of shale after reactive fluid exposure, while extension to field-scale conditions requires further verification under longer creep durations, saturated or continuously reactive conditions, different bedding orientations, and more realistic stress and fluid environments.

Author Contributions: Conceptualization, J.Y. and H.H.; methodology, J.Y. and Z.W.; validation, Z.W. and H.X.; formal analysis, J.Y. and Z.W.; investigation, J.Y., Z.L. and H.X.; resources, H.H., Z.L. and H.X.; data curation, J.Y., Z.L. and Z.W.; writing—original draft preparation, J.Y.; writing—review and editing, H.H., Z.L., Z.W. and H.X.; visualization, J.Y. and Z.W.; supervision, H.H.; project administration, H.H.; funding acquisition, H.H. All authors have read and agreed to the published version of the manuscript.

Funding: This research was funded by the Shaanxi Province Key Research and Development Program, grant number 2024GX-YBXM-505; the National Natural Science Foundation of China, grant number 52474043; and the Joint Funds of the National Natural Science Foundation of China, grant number U23B2089.

Data Availability Statement: The original contributions presented in this study are included in the article. Further inquiries can be directed to the corresponding author.

Conflicts of Interest: Authors Yuan Jiabao and Huang Hai were employed by the Engineering Research Center of Development and Management for Low to Ultra-Low Permeability Oil & Gas Reservoirs in West China, Ministry of Education. Authors Liu Zhengwei and Wang Zhuo were employed by the No.1 Oil Production Plant, PetroChina Changqing Oilfield Company. Author Xu Hongxing was employed by the CCDC Changqing Down Hole Technology Company. All authors declare that the research was conducted in the absence of any commercial or financial relationships that could be construed as potential conflicts of interest.

References

1. Cai, J.; Jiao, X.; Wang, H.; He, W.; Xia, Y. Multiphase fluid-rock interactions and flow behaviors in shale nanopores: A comprehensive review. *Earth-Sci. Rev.* **2024**, *257*, 104884. [CrossRef]
2. Ai, E.; Li, Q.; Liu, Z.; Zhang, B.; Wang, L.; Ma, C. Advanced Trends in Shale Mechanical Inhibitors for Enhanced Wellbore Stability in Water-Based Drilling Fluids. *Minerals* **2024**, *14*, 1197. [CrossRef]
3. Li, Q.; Zhu, D.-Y.; Zhuang, G.-Z.; Li, X.-L. Advanced development of chemical inhibitors in water-based drilling fluids for shale formations. *Pet. Sci.* **2025**, *22*, 1977–1996. [CrossRef]
4. Xu, X.; Chen, C.; Zhou, Y.; Pan, J.; Song, W.; Zhu, K.; Wang, C.; Li, S. Study of the Wellbore Instability Mechanism of Shale in the Jidong Oilfield under the Action of Fluid. *Energies* **2023**, *16*, 2989. [CrossRef]
5. Chang, L.; Wang, H.; Zhuo, L.; Huang, H.; Zou, L.; Wang, Q.; Li, H.; Yu, J. Analysis of Wellbore Stability considering the Interaction between Fluid and Shale. *Geofluids* **2023**, *2023*, 4488607. [CrossRef]
6. Zhuang, Y.; Liu, X.; Chen, Z.; Liang, L.; Zhang, S.; Xiong, J.; Zhang, T. Investigation on effects of water-shale interaction on acoustic characteristics of organic-rich shale in Ordos Basin, China. *J. Pet. Explor. Prod. Technol.* **2024**, *14*, 2753–2767. [CrossRef]
7. Khan, H.J.; Spielman-Sun, E.; Jew, A.D.; Bargar, J.; Kovscek, A.; Druhan, J.L. A critical review of the physicochemical impacts of water chemistry on shale in hydraulic fracturing systems. *Environ. Sci. Technol.* **2021**, *55*, 1377–1394. [CrossRef] [PubMed]
8. Jew, A.D.; Druhan, J.L.; Ihme, M.; Kovscek, A.R.; Battiato, I.; Kaszuba, J.P.; Bargar, J.R.; Brown, G.E. Chemical and reactive transport processes associated with hydraulic fracturing of unconventional oil/gas shales. *Chem. Rev.* **2022**, *122*, 9198–9263. [CrossRef] [PubMed]

9. Li, Q.; Jew, A.D.; Kohli, A.; Maher, K.; Brown, G.E.; Bargar, J.R. Thicknesses of chemically altered zones in shale matrices resulting from interactions with hydraulic fracturing fluid. *Energy Fuels* **2019**, *33*, 6878–6889. [CrossRef]
10. Li, Q.; Jew, A.D.; Brown, G.E.; Bargar, J.R.; Maher, K. Reactive transport modeling of shale-fluid interactions after imbibition of fracturing fluids. *Energy Fuels* **2020**, *34*, 5511–5523. [CrossRef]
11. Khan, H.J.; Ross, C.M.; Druhan, J.L. Impact of concurrent solubilization and fines migration on fracture aperture growth in shales during acidized brine injection. *Energy Fuels* **2022**, *36*, 5681–5694. [CrossRef]
12. Li, S.; Zhang, S.; Xing, H.; Zou, Y. CO_2-brine-rock interactions altering the mineralogical, physical, and mechanical properties of carbonate-rich shale oil reservoirs. *Energy* **2022**, *256*, 124608. [CrossRef]
13. Liu, G.; Shang, D.; Zhang, L.; Xie, S.; Pan, W. Short-term interactions between Longmaxi shale and carbon dioxide-based fracturing fluids. *Heliyon* **2024**, *10*, e38575. [CrossRef] [PubMed]
14. Zhou, H.; Wang, B.; Zhou, F.-J. Mechanical, structural, and mineralogical changes of shale under acid-CO_2-rock interactions and their implications for CO_2 storage. *Pet. Sci.* **2026**, *23*, 1261–1279. [CrossRef]
15. Zhang, S.; Shen, Z.; He, Y.; Zhu, Z.; Ren, Q.; Zhang, L. Pore Structure Alteration of Shale with Exposure to Different Fluids: The Longmaxi Formation Shale in the Sichuan Basin, China. *Minerals* **2023**, *13*, 1387. [CrossRef]
16. Du, J.; Whittle, A.J.; Hu, L.; Divoux, T.; Meegoda, J.N. Mechanical degradation of Longmaxi shale exposed to water-based fluids and supercritical carbon dioxide. *J. Rock Mech. Geotech. Eng.* **2024**, *17*, 3378–3394. [CrossRef]
17. Li, J.; Hu, B.; Sheng, J.; Zhang, Z. Effect of acid corrosion on shear creep behavior of Permian carbonaceous shale in Southwest China. *J. Rock Mech. Geotech. Eng.* **2025**, *18*, 1858–1875. [CrossRef]
18. Zhang, X.; Hu, B.; Li, J.; Huang, L.; Zhang, Z.; Li, B.; Zhong, Z.; Wan, C. Acid corrosion deterioration of carbonaceous shale: Mechanism revealed from shear properties and macro-micro structure. *Constr. Build. Mater.* **2025**, *474*, 141062. [CrossRef]
19. Prakash, R.; Abedi, S. Experimentally informed simulation of creep behavior in shale rocks induced by chemo-mechanical loading. *Rock Mech. Rock Eng.* **2023**, *56*, 6631–6645. [CrossRef]
20. Farooq, U.; Siddiqui, M.A.Q.; Regenauer-Lieb, K.; Roshan, H. Mechanistic insights into damage-driven creep in organic-rich shales. *Rock Mech. Rock Eng.* **2025**, *58*, 13153–13172. [CrossRef]
21. Liu, K.; Rassouli, F.S.; Liu, B.; Ostadhassan, M. Creep behavior of shale: Nanoindentation vs. triaxial creep tests. *Rock Mech. Rock Eng.* **2020**, *54*, 321–335. [CrossRef]
22. Liu, Y.; Yang, C.; Wang, J.; Xiong, Y.; Peng, P. New insights into hydration-induced creep behavior of shale: A comparison study of brittle black shale and clayey oil shale at micro-scale. *Mar. Pet. Geol.* **2022**, *138*, 105554. [CrossRef]
23. Liu, Y.; Burch, A.C.; Bennett, K.C.; Abousleiman, Y.; Borja, R.I. Bridging nanoindentation and triaxial creep tests on a shale. *Acta Geotech.* **2023**, *18*, 6475–6487. [CrossRef]
24. Shi, X.; Jiang, S.; Yang, L.; Tang, M.; Xiao, D. Modeling the viscoelasticity of shale by nanoindentation creep tests. *Int. J. Rock Mech. Min. Sci.* **2020**, *127*, 104210. [CrossRef]
25. Wang, J.; Liu, Y.; Yang, C.; Jiang, W.; Li, Y.; Xiong, Y. Modeling the viscoelastic behavior of quartz and clay minerals in shale by nanoindentation creep tests. *Geofluids* **2022**, *2022*, 2860077. [CrossRef]
26. Siddiqui, M.A.Q.; Roshan, H. Thermodynamic characterization of chemical damage in variably saturated water-active shales. *Rock Mech. Rock Eng.* **2022**, *55*, 5259–5284. [CrossRef]
27. Siddiqui, M.A.Q.; Serati, M.; Regenauer-Lieb, K.; Roshan, H. A thermodynamics-based multi-physics constitutive model for variably saturated fractured sorptive rocks. *Int. J. Rock Mech. Min. Sci.* **2022**, *158*, 105202. [CrossRef]
28. Algazlan, M.; Siddiqui, M.A.Q.; Regenauer-Lieb, K.; Roshan, H. A methodological determination of sorptive poromechanical constitutive coefficients for double porosity shales. *Transp. Porous Media* **2023**, *150*, 753–768. [CrossRef]
29. Xiu, X.; Wang, Y.; Zhou, Y.; Niu, G.; Zhao, S.; Chang, D. Creep Model and Experimental Verification of Sandstone under the Coupled Effect of Chemical Corrosion and Temperature. *Appl. Sci.* **2024**, *14*, 7847. [CrossRef]
30. Liu, W.; Zhang, S.; Huang, X.; Li, J. Nonlinear creep damage model of rock considering alkali corrosion and time effect. *Geomech. Geophys. Geo-Energy Geo-Resour.* **2025**, *11*, 68. [CrossRef]
31. Ju, W.; You, Y.; Chen, Y.; Feng, S.; Xu, H.; Zhao, Y.; Liu, B. Nanoscale pore structure and fractal characteristics of the continental Yanchang Formation Chang 7 shale in the southwestern Ordos Basin, central China. *Energy Sci. Eng.* **2019**, *7*, 1188–1200. [CrossRef]
32. Ling, K.; Wang, Z.; Cao, Y.; Liu, Y.; Dong, L. Clay Mineral Characteristics and Smectite-to-Illite Transformation in the Chang-7 Shale, Ordos Basin: Processes and Controlling Factors. *Minerals* **2025**, *15*, 951. [CrossRef]

Disclaimer/Publisher's Note: The statements, opinions and data contained in all publications are solely those of the individual author(s) and contributor(s) and not of MDPI and/or the editor(s). MDPI and/or the editor(s) disclaim responsibility for any injury to people or property resulting from any ideas, methods, instructions or products referred to in the content.